

**Moist Vortex Dynamics of Axisymmetric Tropical Cyclones Before Reaching Symmetric  
Neutrality - Part I: A Generalized Tangential Wind Formula**

Chau-Lam Yu<sup>1,2</sup>

<sup>1</sup>New York State Mesonet, SUNY University at Albany, Albany, NY, USA

<sup>2</sup>Department of Atmospheric and Environmental Sciences, SUNY University at Albany,  
Albany, NY, USA

Submitted to *Journal of the Atmospheric Sciences*<sup>1</sup>

Submitted

February 12<sup>th</sup>, 2025

*Corresponding author address:* Chau-Lam Yu, New York State Mesonet, ETEC Building -  
Harriman Campus, 1200 Washington Avenue, Room 360E, Albany, NY 12226

E-mail: [cyu7@albany.edu](mailto:cyu7@albany.edu)

---

<sup>1</sup> This Work has been submitted to Journal of the Atmospheric Sciences. Copyright in this Work may be transferred without further notice.

## Abstract

The potential intensity (PI) theory of tropical cyclones (TCs) provides a reasonable estimate of the maximum intensity of a steady-state TC in a quiescent environment. The traditional PI theory relies on the symmetric neutrality (SN) assumption, where the isolines of absolute angular momentum ( $M$ ) are parallel to the saturation entropy ( $s^*$ ) surfaces within the eyewall updraft. When the SN is not valid, there is currently no quantitative theory that explicitly describes how these surfaces directly relate to the maximum tangential wind ( $v_{\max}$ ) near the surface.

In this study, the PI theory is revisited without making the SN assumption. Under non-SN conditions, it is found that the balance between the centrifugal torque and baroclinic torque provides a strong constraint on the vortex structure and balanced intensity. Specifically, it is shown that the gradient between  $s^*$  and  $M$  along constant temperature ( $T$ ) throughout the saturated eyewall determines the structure of the  $M$  surface and the balanced intensity at the low level. The same technique can be applied to obtain the generalized terms that correspond to the unbalanced component. It is shown that this generalized  $v_{\max}$  equation is the natural extension of the traditional PI formula into the non-symmetric neutrality regime.

Verifying against axisymmetric simulations, it is shown that the generalized  $v_{\max}$  equation can accurately quantify the various contributions to  $v_{\max}$  during the rapid intensification process. The implications of these findings on the TC rapid intensification, such as the TC inner-core structure and the upper-tropospheric mixing process, are examined.

## 1. Introduction

As the long-lasting eyewall convection of a tropical cyclone (TC) transports high-entropy air into the upper troposphere, convective and symmetric instabilities are released and eventually neutralized, resulting in a steady-state vortex structure with zero moist potential vorticity (Emanuel 1986, E86 hereafter). This steady-state vortex structure is symmetrically neutral, where the isolines of saturation entropy  $s^*$  and absolute angular momentum  $M$  are congruent to streamfunction  $\psi$  in the free troposphere. The symmetric neutrality (SN) assumption, along with gradient wind and hydrostatic balance, has long been known to constrain the steady-state structure and intensity of tropical cyclones (E86; Emanuel and Rotunno 2011, ER11 hereafter; D. K. Lilly 1979, 1986 (unpublished manuscripts); Tao et al. 2020). In addition, the SN condition is the core assumption of our theoretical understanding of the impacts of dissipative heating (Bister and Emanuel 1997), intrusion of low entropy air into TC inner core, i.e., ventilation (Tang and Emanuel 2010; 2012a,b), the potential size of TCs (Wang et al. 2022), etc. Building upon the SN and steady-state assumptions, Bryan and Rotunno (2009a,b, BR09a,b) derived a quantitative estimate for the contribution of the unbalanced processes on the maximum tangential wind at and above the boundary layer top.

In the past decade, research efforts have gradually shifted from steady-state centric to focusing more on TC intensification. Emanuel (2012, E12) demonstrated that assuming congruence between  $s^*$  and  $M$  surfaces in the free troposphere, while allowing for crossing between these surfaces and streamfunction isolines, permits the temporal evolution of intensity, yielding a time-dependent model that captures the later intensification period. A similar time-dependent model was later derived using thermodynamic cycle (Ozawa and Shimokawa 2015), even though SN was assumed implicitly<sup>2</sup>. Despite this advancement, the E12 time-dependent model has limitations, as it does not accurately capture the early intensification evolution and requires a subjectively determined “ignition time” to match the analytic solution with numerical model simulations. Consequently, it cannot be used to predict the onset timing of intensification.

These shortcomings of the E12 model exposed the fundamental limitations of the SN assumption. As confirmed by other studies (Peng et al. 2018, 2019), the SN assumption is not valid until the later stages of the intensification period. Recent developments in time-dependent models

---

<sup>2</sup> The cyclic return of parcels to initial state is true only at steady state. Since  $M$  and  $s^*$  are approximately conserved in free troposphere, the steady state requirement thus forces both variables to be congruent with  $\psi$ . Hence, SN is assumed implicitly.

have attempted to incorporate the effects of Non-SN by introducing several ad-hoc parameters (Wang et al. 2021a,b; Li et al. 2024). While those empirically determined parameters help to identify the dependence of intensification rate that matches the numerical simulations, it is difficult to guarantee that the resulting dependence is universally true and not specific only to the set of numerical experiments. More importantly, it is challenging to discern the underlying physics that determines specific values of the parameters.

This recent development motivates a more thorough examination of the axisymmetric moist vortex dynamics before the SN assumption becomes valid. Many questions surrounding the dynamics of non-symmetrically neutral (non-SN) vortices remain unanswered. For instance, the PI theory showed that the balanced boundary layer top tangential wind is dynamically linked to the total derivative of  $s^*$  w.r.t  $M$ , i.e.,  $ds^*/dM$ , and the temperature difference between the boundary layer top and the outflow level. However, the term  $ds^*/dM$  is mathematically well-defined only when  $s^*$  and  $M$  isolines are congruent. When the SN condition is not met, it is unclear how the gradient between  $s^*$  and  $M$  should be computed such that it is dynamically linked to the tangential wind maximum at the low level. Moreover, the exact role of the temperature difference between the boundary layer top and outflow level is unclear in the non-SN regime. To address these questions, in this study, we revisit the derivation of the PI theory without making the SN assumption to uncover how these established results extend into the non-SN regime.

The primary objective of the first part is to establish a fundamental framework that captures the essential moist vortex dynamics for non-SN vortices. Using the radial and vertical momentum equations and the modified first law of thermodynamics, several fundamental results are obtained without making SN assumption, including a new energetic property that constrains the structure of a balanced vortex and a fully generalized (diagnostic) tangential wind formula that encompasses both the balanced and unbalanced components under non-SN condition. Building upon the findings of the first part, the second part of this work will incorporate the conservation principles of absolute angular momentum, moist entropy, and mass continuity to derive a time-dependent model. It should be acknowledged that asymmetric processes are an intrinsic component of the TC intensification (Persing et al. 2013). We choose to focus on the axisymmetric modeling framework since it, to a large extent, can capture the major component of the TC intensification and can provide important insight into underlying dynamics.

The remainder of this paper is organized as follows. We derive the theoretical findings in section 2, followed by a description of the numerical experiments and the evaluation methods in section 3. Section 4 presents a detailed verification of the theoretical results, while section 5 discusses the implications of these findings. Section 6 summarizes the major findings and limitations of this work.

## 2. Theory

### a. The balanced component

For direct comparison with the results from E86 and ER11, we first consider the balanced case in gradient wind and hydrostatic balance. The fully generalized form without balanced assumptions will be derived in section 2b. Under the radius-pressure  $(r, p)$  coordinate and assuming axisymmetry, the gradient wind and hydrostatic balance equations may be written as

$$\frac{\partial \phi}{\partial r} = \frac{M^2}{r^3} - \frac{1}{4} f^2 r \quad (1)$$

$$\frac{\partial \phi}{\partial p} = -\alpha_d \quad (2)$$

where  $M = rv + \frac{1}{2} fr^2$  the absolute angular momentum,  $\phi$  the geopotential;  $\alpha_d = 1/\rho_d$  the dry air specific volume. As discussed in BR09b, the above formulation neglected the contributions of moisture and hydrometeors to the value of total density  $\rho$  and pressure  $p$  of moist air. The thermal wind can be obtained by cross-differentiating (1) with respect to  $p$  and (2) with respect to  $r$  and taking their difference

$$-\frac{1}{r^3} \frac{\partial M^2}{\partial p} = \frac{\partial \alpha_d}{\partial r} \quad (3)$$

Similar to E86, we assume the air within the eyewall updraft is saturated and define saturation entropy  $s^* = c_p \ln T - R_d \ln p + \frac{L_v q^*}{T}$ , where  $T$  the temperature,  $q^*$  the saturation vapor mixing ratio,  $c_p$  the heat capacity at constant pressure,  $R_d$  the ideal gas constant of dry air, and  $L_v$  the latent heat of vaporization. This formulation of  $s^*$  also neglected the contribution of vapor to the pressure of moist air, so that  $p \approx p_d$  (pressure of dry air). In section 2c, we will derive a correction term to account for the effects of moisture density and pressure on the intensity estimate. Writing

$\left(\frac{\partial \alpha_d}{\partial r}\right)_p$  as  $\left(\frac{\partial \alpha_d}{\partial s}\right)_p \left(\frac{\partial s^*}{\partial r}\right)_p$  and combining with Maxwell relation  $\left(\frac{\partial \alpha_d}{\partial s}\right)_p = \left(\frac{\partial T}{\partial p}\right)_{s^*}$  (E86; BR09b)

and dividing both sides with  $\left(\frac{\partial M}{\partial r}\right)_p$  yields

$$\frac{2M}{r^3} \left(\frac{\partial r}{\partial p}\right)_M = \left(\frac{\partial T}{\partial p}\right)_{s^*} \left(\frac{\partial s^*}{\partial M}\right)_p \quad (4)$$

E86 and many subsequent studies proceeded by making the SN assumption, which is strictly true only when the TC evolves into a steady-state. It is found that simplification of equation (4) can be achieved without making the SN assumption. As shown in appendix A, the term  $\left(\frac{\partial T}{\partial p}\right)_{s^*} \left(\frac{\partial s^*}{\partial M}\right)_p$  is a Jacobian matrix determinant for transformation from  $(M, p)$  space to  $(s^*, T)$  space, denoted as  $J\left(\frac{s^*, T}{M, p}\right)$ . Based on the theorem of coordinate transformation,  $\left(\frac{\partial T}{\partial p}\right)_{s^*} \left(\frac{\partial s^*}{\partial M}\right)_p dMdp = ds^*dT$  where  $dMdp$  and  $ds^*dT$  are the differential elements in  $(M, p)$  and  $(T, s^*)$  spaces. Therefore, by multiplying both sides of (4) with the differential element  $dMdp$  in  $(M, p)$  space, it can be simplified as

$$\begin{aligned} \frac{2M}{r^3} \left(\frac{\partial r}{\partial p}\right)_M dMdp &= \left(\frac{\partial T}{\partial p}\right)_{s^*} \left(\frac{\partial s^*}{\partial M}\right)_p dMdp \\ dM^2 d\left(-\frac{1}{2r^2}\right) &= ds^*dT \end{aligned} \quad (5)$$

Equation (5) is essentially the integral form of (4). Mathematically, it states that for any region of a balanced vortex, the corresponding areas in  $\left(-\frac{1}{2r^2}, M^2\right)$  and  $(s^*, T)$  spaces must be the same

$$\iint_D dM^2 d\left(-\frac{1}{2r^2}\right) = \iint_D dT ds^* \quad (6)$$

where  $D$  is an arbitrary saturated region within a balanced vortex in physical space. Physically, equation (5) represents the balance between the azimuthal torque of centrifugal force (area in  $\left(-\frac{1}{2r^2}, M^2\right)$  space) and baroclinic torque (area in  $(s^*, T)$  space). Using Stoke's theorem, the area integral of azimuthal torque equals the loop integral of the net (virtual) work done by the associated force. Therefore, equation (5) can also be interpreted as the balance between the net (virtual) work done by the centrifugal force and pressure gradient force along the closed boundary  $\partial D$ .

Direct verification of (5) and (6) requires simultaneous transformations of physical fields from  $(r, p)$  physical space to  $(M^2, -1/2r^2)$  and  $(s^*, T)$  spaces, which can be challenging due to the complex structure of  $M$  and  $s^*$  fields during intensification. However, we note that (6) is also valid for a dry balanced vortex by replacing  $s^*$  with dry entropy  $s$ . Figure 1 shows a verification

example for a dry balanced vortex. By arbitrarily selecting two pairs of  $M$  ( $1 \times 10^6$  and  $2.55 \times 10^6$   $\text{m}^2 \text{s}^{-1}$ ) and  $s$  (2475 and 2530  $\text{J kg}^{-1} \text{K}^{-1}$ ) isolines, which define an arbitrary region  $D$ , we confirm that the corresponding regions in  $(-1/2r^2, M^2)$  space and  $(s, T)$  space both have areas of about 211.3 [ $\text{J kg}^{-1}$ ], thus verifying equations (10) and (11).

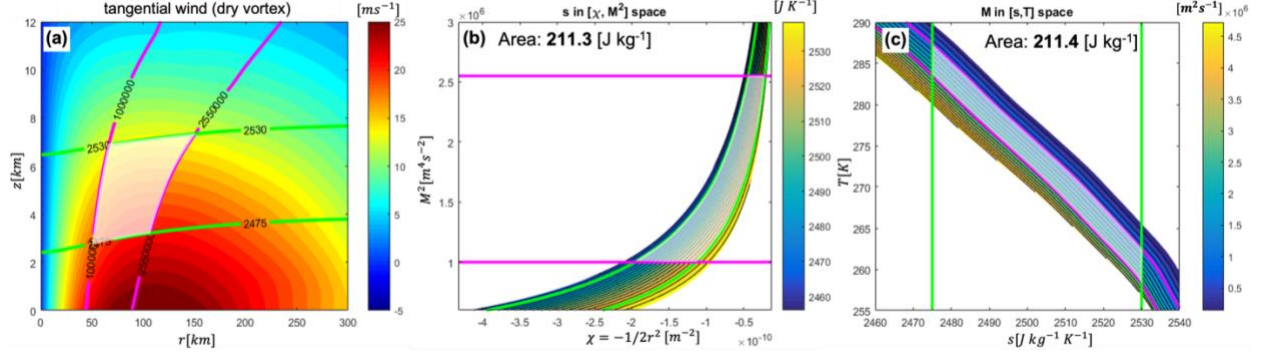


**Fig. 1:** (a) The tangential wind of a balanced, axisymmetric dry vortex. Magenta lines show the two  $M$  surfaces ( $10^6$  and  $2.55 \times 10^6$   $\text{m}^2 \text{s}^{-1}$ ), while green lines show the two  $s$  surfaces (2475 and 2530  $\text{J kg}^{-1} \text{K}^{-1}$ ). The whitened portion is the region of interest. (b) Dry entropy  $s$  in  $(-1/2r^2, M^2)$  space. The same region of interest (whitened) has an area of 211.3 [ $\text{J kg}^{-1}$ ]. (c) is similar to (b), but for the  $M$  in  $(s, T)$  space, where the region of interest has an area of 211.4 [ $\text{J kg}^{-1}$ ].

We will now show that, without relying on the SN assumption, the energetic balance property (5) constrains the structure of the  $M$  surfaces and determines the balanced tangential wind maximum at the low level. If we return to equation (4) and use the Jacobian identity

$$\left(\frac{\partial T}{\partial p}\right)_{s^*} \left(\frac{\partial s^*}{\partial M}\right)_p = \left(\frac{\partial T}{\partial p}\right)_M \left(\frac{\partial s^*}{\partial M}\right)_T \quad (\text{i.e., A.3a and A.3b}) \quad \text{to rewrite (4) as}$$

$$\frac{2M}{r^3} \left(\frac{\partial r}{\partial p}\right)_M = \left(\frac{\partial T}{\partial p}\right)_M \left(\frac{\partial s^*}{\partial M}\right)_T \quad (7)$$

Dividing both sides of (7) with  $\left(\frac{\partial T}{\partial p}\right)_M$ , we show that

$$\frac{2M}{r^3} \left(\frac{\partial r}{\partial T}\right)_M = \left(\frac{\partial s^*}{\partial M}\right)_T \quad (8)$$

Equation (8) explicitly relates the inverse slope of  $M$  surfaces in  $(r, T)$  space, i.e.,  $\left(\frac{\partial r}{\partial T}\right)_M$ , to slope of temperature surface in  $(M, s^*)$  space, i.e.,  $\left(\frac{\partial s^*}{\partial M}\right)_T$ . This relationship is the generalization of how

$\frac{ds^*}{dM}$  constrains the shape of an  $M$  surface under symmetric neutrality (E86). The physical picture of (8) is that as the  $M$  surfaces of a balanced vortex develop a curved structure towards the TC inner core, the differential tangential wind along the  $M$  surfaces result in an azimuthal torque of the

centrifugal force, as shown in Fig. 2a. To balance this centrifugal torque, a baroclinic torque in the opposite direction (Fig. 2b) must exist by developing a radial gradient in density. In  $(M, s^*)$  space, this density gradient is manifested as variation in temperature along constant  $s^*$ , which determines the slope of the temperature isolines in the  $(M, s^*)$  space, i.e.,  $\left(\frac{\partial s^*}{\partial M}\right)_T$ .

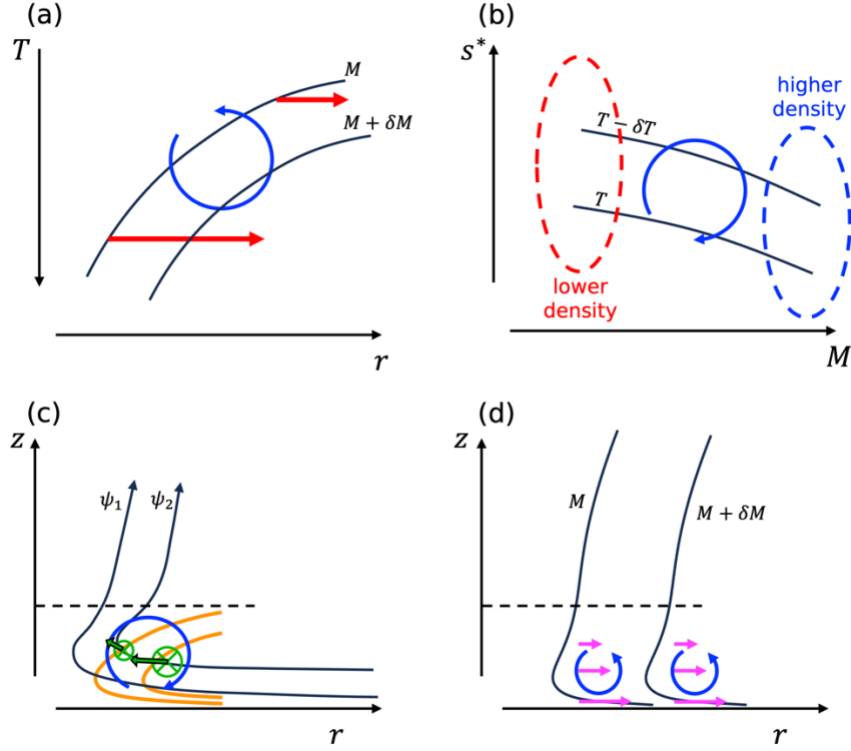


**Fig. 2:** Schematic diagrams illustrating (a) the azimuthal torque (blue circular arrow) of the centrifugal force (red arrows) associated with curved  $M$  surfaces (black isolines) in  $(r, T)$  space; (b) the baroclinic torque (blue circular arrow) induced by the radial gradient of temperature (and density indicated by red and blue dashed ellipses); (c) the azimuthal torque (blue circular arrow) induced by the convergence of azimuthal vorticity flux (green arrows and cross signs); (d) azimuthal torque (blue circular arrow) induced by radial and vertical friction (magenta arrows). Orange contours in (c) indicate radial velocity isolines. The black dashed line in (c) and (d) indicate the boundary layer top.

If we now integrate (8) along a  $M$  isoline from some temperature  $T_b$  at the boundary layer to the outflow temperature  $T_o$  where  $v = 0$ , we have

$$\int_{T_b}^{T_o} \frac{2M}{r^3} \left(\frac{\partial r}{\partial T}\right)_M dT = \int_{T_b}^{T_o} \left(\frac{\partial s^*}{\partial M}\right)_T dT$$

$$\frac{v_b}{r_b} = \int_{T_b}^{T_o} \left( \frac{\partial s^*}{\partial M} \right)_T dT \quad (9)$$

Equation (9) shows that the balanced tangential wind at the low level is proportional to the accumulation of  $\left( \frac{\partial s^*}{\partial M} \right)_T$ , i.e.,  $\frac{\partial s^*}{\partial M}$  along constant temperature  $T$ , from  $T_b$  to  $T_o$ . Equation (9) is the natural extension of equation (12) of E86 ( $\frac{M}{r^2} = -\frac{ds^*}{dM}(T_b - T_o)$ ) into the non-SN regime. Under symmetric neutrality,  $\left( \frac{\partial s^*}{\partial M} \right)_T = \frac{ds^*}{dM}$  and is only a function of  $M$ , reducing (9) to  $\frac{v_b}{r_b} = -\frac{ds^*}{dM}(T_b - T_o)$ .

It is worth noting that when symmetric neutrality is not assumed,  $\left( \frac{\partial s^*}{\partial M} \right)_T$  is not just a function of  $M$ , but also depends on  $T$ . The structural evolution of  $\left( \frac{\partial s^*}{\partial M} \right)_T$  as a function of  $T$  within the eyewall region will be examined in a later section.

If we further treat  $T_b$  and  $T_o$  as *predetermined constants* for a given  $M$  surface (based on the desired  $z_b$  and outflow radius of the  $M$  surface), we can simplify (9) by exchanging the integration and differentiation operators using the Leibniz rule of integration

$$\frac{v_b}{r_b} = \frac{d}{dM} \left( \int_{T_b}^{T_o} s^* dT \right) \quad (10)$$

Equation (10) allows the evaluation of  $v_b$  without computing partial derivatives fixing temperature. It also shows that the distribution of  $s^*$  along  $M$  surfaces directly determines  $v_b$  at the low level. Specifically, for a narrow region bounded by two adjacent  $M$  surfaces, the difference in the entropy integral  $\int_{T_b}^{T_o} s^* dT$  between these two  $M$  surfaces is proportional to the balanced  $v_b$  near the surface. This result has several implications. First, under non-SN condition, a saturated TC eyewall is a *frontal zone of integrated saturation entropy across  $M$  surfaces*, a generalization of the findings derived by Emanuel (1997). Second, equation (10) indicates that any process that can reduce the gradient of the entropy integral across  $M$  surfaces can result in the weakening of the balanced intensity. One such process is ventilation, where environmental dry air is injected into the TC inner core. Despite assuming saturation, the above inference does not rely on the SN assumption, which was one of the core assumptions of the ventilation theory (Tang and Emanuel 2009).

The derivations of (9) and (10) use the equivalent forms of a Jacobian matrix determinant (Appendix A). As shown in Appendix B, it is possible to derive (9) and (10) entirely based on the energetic property (5) alone.

*b. General form in height coordinate*

A more general derivation of the tangential wind formula in height coordinate, which includes the nonlinear advection of radial and vertical momentum and boundary layer friction, is provided in Appendix C. The inclusion of these processes results in additional terms:

$$\frac{v_b}{r_b} = \int_{T_b}^{T_o} \left( \frac{\partial S^*}{\partial M} \right)_T dT + \int_{\tilde{\eta}_b/r_b}^{\tilde{\eta}_o/r_o} \left( \frac{\partial \psi}{\partial M} \right)_{\tilde{\eta}/r} d\left( \frac{\tilde{\eta}}{r} \right) - \int_{r_b}^{r_o} \left( \frac{\partial F_r}{\partial M} \right)_r dr - \int_{z_b}^{z_o} \left( \frac{\partial F_z}{\partial M} \right)_z dz \quad (11)$$

, where  $F_r$  and  $F_z$  are the radial and vertical momentum forcings;  $\psi$  is the nondivergent streamfunction;  $\tilde{\eta} = \frac{1}{\rho} \left( \frac{\partial u}{\partial z} - \frac{\partial w}{\partial r} \right)$  with  $\rho$  the density of moist air. Equations (11a,b) summarize the different processes contributing to the azimuthal torque balance to maintain the curved structure of  $M$  surfaces of a saturated non-SN vortex. As explained in appendix C, in addition to the balanced term, the second term of the R.H.S represents the effect of azimuthal torque induced by azimuthal vorticity flux convergence, whereas the sum of third and fourth terms represent the effect of frictional torque, as illustrated in Fig. 2c and 2d.

Focusing on the 2<sup>nd</sup> term, if we assume symmetric neutrality above the boundary layer where  $F_r = F_z = 0$ ,  $\left( \frac{\partial \psi}{\partial M} \right)_{\tilde{\eta}/r}$  then becomes  $\frac{d\psi}{dM}$  and is only a function of  $M$ . Therefore,  $\int_{\tilde{\eta}_b/r_b}^{\tilde{\eta}_o/r_o} \left( \frac{\partial \psi}{\partial M} \right)_{\tilde{\eta}/r} d\left( \frac{\tilde{\eta}}{r} \right) = \frac{d\psi}{dM} \left( \frac{\tilde{\eta}_o}{r_o} - \frac{\tilde{\eta}_b}{r_b} \right) \approx -\frac{d\psi}{dM} \frac{\tilde{\eta}_b}{r_b}$ , which is precisely the unbalanced term derived by BR09b (their equation 19).

BR09b neglected boundary layer friction in deriving their equation (20). This is because, at steady state, SN condition is true only above the boundary layer where  $F_r$  and  $F_z$  vanish. Since the SN assumption is now relaxed in the present study, the derivation of (11) includes boundary layer frictional terms and can be applied to within the TC boundary layer. It should, therefore, be noted that it is the sum of the  $\tilde{\eta}$  term (2<sup>nd</sup> term) and boundary layer friction term (3<sup>rd</sup> and 4<sup>th</sup> terms) in (11) together that represents the unbalanced, supergradient wind component (Montgomery and Smith 2017; Rotunno 2022).

*c. A correction term to the balanced component*

As discussed in BR09a, E86 neglected the contribution of vapor to the density and pressure of moist air. In addition, the Maxwell relation,  $\left(\frac{\partial \alpha}{\partial s}\right)_p = \left(\frac{\partial T}{\partial p}\right)_{s^*}$  is derived based on the modified first law of thermodynamics,  $Tds^* = c_v dT + p d\alpha + L_v dq^*$ , which neglects the temperature variation  $(-\frac{L_v q^*}{T} dT)$  in the latent heat release, a long-standing approximation in previous studies (E86; Emanuel 1994; Bryan 2008). As shown in Appendix D, the error induced by these approximations on the balanced intensity can be corrected by the following correction term

$$\left(\frac{v_b}{r_b}\right)_{correction} = - \int_{T_b}^{T_o} \gamma \left(\frac{\partial s^*}{\partial M}\right)_T dT \quad (12)$$

, where  $\gamma = \frac{R_r \beta}{1 + \beta}$  with  $\beta = \frac{L_v q^*}{R_d T}$  and  $R_r = \frac{R_d}{R_v} \approx 0.622$ . The above correction shares some similarities to Emanuel (1988) but is different in that the total water content is not assumed to be a function of  $M$  alone. Combining with (11), the final form of the tangential wind formula is

$$\frac{v_b}{r_b} = \int_{T_b}^{T_o} \left(\frac{\partial s^*}{\partial M}\right)_T (1 - \gamma) dT - \int_{\tilde{\eta}_b/r_b}^{\tilde{\eta}_o/r_o} \left(\frac{\partial \psi}{\partial M}\right)_{\tilde{\eta}/r} d\left(\frac{\tilde{\eta}}{r}\right) - \int_{r_b}^{r_o} \left(\frac{\partial F_r}{\partial M}\right)_r dr - \int_{z_b}^{z_o} \left(\frac{\partial F_z}{\partial M}\right)_z dz \quad (13)$$

, where the first term is referred to as the bias-corrected balanced wind component. If the SN condition is assumed,  $\left(\frac{\partial s^*}{\partial M}\right)_T$  becomes  $\frac{ds^*}{dM}$  and is constant along the integration path. Further assuming  $M \approx r_b v_b$ , the bias-corrected maximum potential intensity (MPI) under SN condition is

$$\begin{aligned} v_{b_{MPI}}^2 &= M \frac{ds^*}{dM} \int_{T_b}^{T_o} (1 - \gamma) dT \\ &= -(\overline{1 - \gamma}) M \frac{ds^*}{dM} (T_b - T_o) \end{aligned} \quad (14)$$

, where  $\overline{1 - \gamma} \equiv \frac{1}{T_o - T_b} \int_{T_b}^{T_o} 1 - \gamma dT$ . If we define  $v_{E86}^2 = -M \frac{ds^*}{dM} (T_b - T_o)$ , the bias-corrected maximum intensity is  $v_{b_{MPI}}^2 = (\overline{1 - \gamma}) v_{E86}^2$ .

### 3. Methods of evaluation

*a. Numerical model simulations*

To verify the results in section 2, we use the Cloud Model 1 (CM1; Bryan and Fritsch 2002), version 20.1, to conduct numerical simulations using the “default” axisymmetric TC setting. This

setting is similar to the second configuration in Bryan (2012), except that a modified Rankine vortex profile is used:

$$v_0(r) = \begin{cases} v_m \left( \frac{r}{r_{m1}} \right) & r < r_{m1} \\ v_m \left( \frac{r}{r_{m1}} \right)^{-0.35} & r_{m1} \leq r < r_{m2} \\ w_2 \times v_m \left( \frac{r}{r_{m1}} \right)^{-0.35} + w_3 \times \frac{v_m}{2} \left( 1 - \frac{r - r_{m2}}{r_{m3} - r_{m2}} \right) & r_{m2} \leq r < r_{m3} \\ 0 & r \geq r_{m3} \end{cases} \quad (15)$$

where  $v_m = 15 \text{ ms}^{-1}$  and  $r_{m1} = 75 \text{ km}$  are the initial maximum tangential wind and radius of maximum wind;  $r_{m2} = 200 \text{ km}$  and  $r_{m3} = 500 \text{ km}$ ;  $w_3 := \frac{r - r_{m2}}{r_{m3} - r_{m2}}$  and  $w_2 := 1 - w_3$ . Given the surface wind profile, the full tangential wind is obtained with  $v_m$  decaying linearly from  $15 \text{ ms}^{-1}$  at the surface to  $0 \text{ ms}^{-1}$  at  $z = 15 \text{ km}$ . The moist tropical sounding (Dunion 2011) and a sea surface temperature of  $28 \text{ }^\circ\text{C}$  are used to initialize the simulation. To better conserve saturation entropy, the Rotunno-Emanuel (1987) simple water-only scheme is used.

The total domain size of the simulation is  $1500 \text{ km} \times 25 \text{ km}$ . Horizontal grid spacing  $\Delta r = 500 \text{ m}$  is used within  $350 \text{ km}$  radius, beyond which  $\Delta r$  is stretched to a maximum value of  $4 \text{ km}$  at  $r = 1500 \text{ km}$ . A variable vertical grid spacing is used below  $z = 5375 \text{ m}$  with a maximum  $\Delta z = 200 \text{ m}$ , yielding a total of 141 vertical levels.

Following the suggested setting of Bryan (2012),  $C_E$  is set to  $1.2 \times 10^{-3}$  (Drennan et al. 2007), while we use the “default” CM1 setting for  $C_D$ , defined based on Fairall et al. (2003) at low wind conditions and capped at  $2.4 \times 10^{-3}$ . Similar to previous studies, we do not use a realistic radiation scheme but include the Newtonian cooling term in the potential temperature equation that mimics the radiative cooling effect, which is capped at  $2 \text{ K day}^{-1}$ .

Because of the large variability during the TC intensification, a set of 11-member ensemble simulations are performed to remove the random fluctuations in the intensification process. First, a control simulation (CTRL) is performed using the setting described above. At hour 21, random perturbations of the potential temperature of  $0.1 \text{ K}$  magnitude are added to the inner-core region with  $r \leq 100 \text{ km}$  and  $z \leq 15 \text{ km}$  to create 10 perturbed simulations, forming the 11-member ensemble. Perturbations are added at hour 21 instead of at the initial condition because this time is nearly at the end of the boundary layer spin-up process and is before the onset of the intensification process. As such, all perturbed members intensify with similar onset timing of RI and

intensification rate as the CTRL, thus allowing the removal of random fluctuation in the intensification process.

*b. Evaluation of path integrals*

One additional challenge is that  $\left(\frac{\partial s^*}{\partial M}\right)_T$  (or  $\left(\frac{\partial \psi}{\partial M}\right)_{\tilde{\eta}/r}$ ) may have singularities along the integration path. Fortunately, we showed in Appendix E that these singularities can always be regularized such that the integrals in (11) are always integrable. Specifically, the following expressions are the optimal regularizations for  $\left(\frac{\partial s^*}{\partial M}\right)_T$  and  $\left(\frac{\partial \psi}{\partial M}\right)_{\tilde{\eta}/r}$

$$\left(\overline{\frac{\partial s^*}{\partial M}}\right)_T := \frac{1}{\delta T} \int_{l_i - \frac{\delta l}{2}}^{l_i + \frac{\delta l}{2}} J\left(\frac{s^*, T}{r, z}\right) \frac{dl}{|\nabla M|} \quad (16a)$$

$$\left(\overline{\frac{\partial \psi}{\partial M}}\right)_{\tilde{\eta}/r} := \frac{1}{\delta(\tilde{\eta}/r)} \int_{l_i - \frac{\delta l}{2}}^{l_i + \frac{\delta l}{2}} J\left(\frac{\psi, \tilde{\eta}/r}{r, z}\right) \frac{dl}{|\nabla M|} \quad (16b)$$

where  $l_i$  is the  $i$ -th grid point along the desired  $M$  surface (parameterized by path length  $l$ ). When singularity does not occur,  $\left(\overline{\frac{\partial s^*}{\partial M}}\right)_T$  and  $\left(\overline{\frac{\partial \psi}{\partial M}}\right)_{\tilde{\eta}/r}$  equal to their averaged values between  $[l_i - \frac{\delta l}{2}, l_i + \frac{\delta l}{2}]$ . When singularity occurs within  $[l_i - \frac{\delta l}{2}, l_i + \frac{\delta l}{2}]$ ,  $\left(\overline{\frac{\partial s^*}{\partial M}}\right)_T$  and  $\left(\overline{\frac{\partial \psi}{\partial M}}\right)_{\tilde{\eta}/r}$  enable the accurate integration across the singularity. Because (16a,b) can be used regardless of the presence of singularity, they will be used to compute the first and second terms of (13) in the subsequent analysis.

## 4. Results

*a. Timing of peak intensification rate and intensification period*

Since the main focus of the analysis is on the intensification period, we first identify the timing of the maximum intensification rate ( $t_{RI}$ ). For each ensemble member, a 12-hourly running average is applied to the maximum tangential wind ( $v_{max}$ ) time series (Fig. 3a) to remove the short-term intensity fluctuations. The time derivative of the smoothed  $v_{max}$  time series is then computed to determine the  $t_{RI}$  of each ensemble member. The intensification period of each member is defined as the 24-hour period centered at  $t_{RI}$ . As shown in Fig. 3b,c, when composited

relative to  $t_{RI}$ , the ensemble-mean intensification rate shows a clean peak at  $t_{RI}$  with persistent increase in  $v_{max}$  over the 24-hour window.

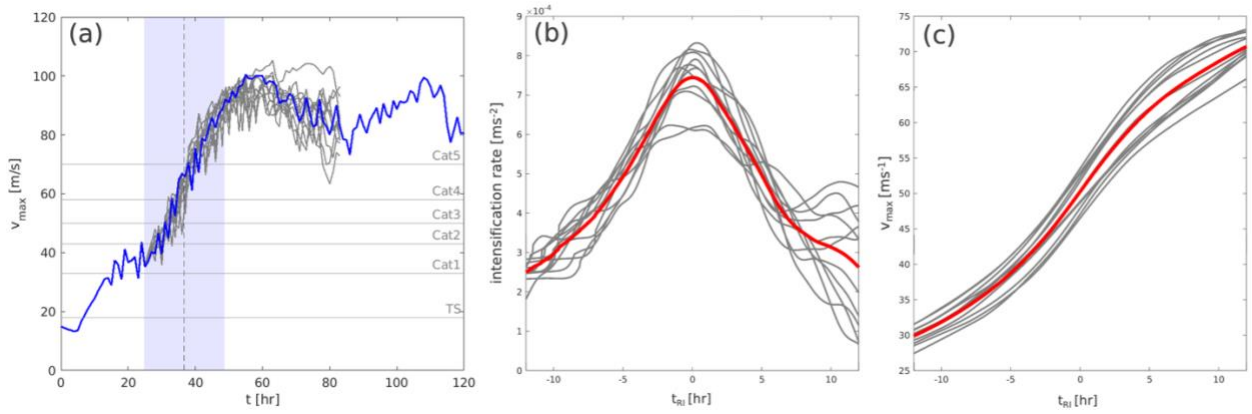


**Fig. 3:** (a) Time series of the  $v_{max}$  of the CTRL (blue) and perturbed (grey) members. (b) Composite of 12-hourly smoothed intensification rate of all members with respect to their  $t_{RI}$ . The composite mean is shown in red, while each ensemble member is shown in grey. (c) is the same as (b), but for 12-hourly smoothed  $v_{max}$  time series.

### b. Evaluation of the generalized tangential wind formula

We now focus on evaluating (13) during the 24-hour intensification time period. For a given time  $t$  during the intensification period, a 3-hour time averaging centered at  $t$  will be applied to all physical fields to remove short-term fluctuation. These temporally-averaged fields are then used to determine the appropriate  $M$  surfaces and the computation of each term in equation (13). It is important to note that the  $J\left(\frac{\psi, \tilde{\eta}/r}{r, z}\right)$  term in (16b) is nonlinear, and therefore is first computed using instantaneous fields and then temporally averaged.

Given that the derivation of the balanced wind component (9) relies on saturation condition and that diabatic heating release is an essential forcing that drives TC secondary circulation and intensification, the set of  $M$  surfaces are chosen to maximize the amount of diabatic heating along the surfaces. Firstly, the averaged density-weighted diabatic heating between  $z = 2$  km and the outflow radius is computed for all  $M$  surfaces at the vicinity of the the eyewall updraft

$$Q_M = \frac{\int_{z=2 \text{ km}}^{z=z_o} \rho Q dl}{\int_{z=2 \text{ km}}^{z=z_o} dl} \quad (17)$$

where  $Q$  is the diabatic forcing from microphysics scheme. The  $M$  surface with the maximum  $Q_M$  is chosen ( $M_{maxQ}$ ). Then, 50  $M$  surfaces within the  $\pm 1$  km radial range of the  $M_{maxQ}$  surface at  $z$

= 2 km are sampled. To ensure the validity of the saturation condition, we compute the averaged relative humidity deficit ( $RH_{deficit}$ ) along the 50  $M$  surfaces

$$RH_{deficit} = \frac{\int_{z=750m}^{z=z_o} (100\% - RH) dl}{\int_{z=750m}^{z=z_o} dl} \quad (18)$$

, where  $RH$  is the relative humidity.  $M$  surfaces that have  $RH_{deficit} \geq 2\%$  are discarded.

Fig. 4 shows the distribution of the selected  $M$  surfaces (gray) at the time of  $t_{RI}$ . It is noted that while the majority of the selected  $M$  surfaces pass through the saturated diabatic heating region, they are located at the slight inward side of the maximum tangential wind jet core (Fig. 4b), having  $v_m$  at  $z = 750$  m about  $5 \text{ ms}^{-1}$  lower than the maximum tangential wind at that level. In contrast, the  $M$  surface that passes through the maximum tangential wind jet core (blue) becomes strongly subsaturated immediately above 2 km and are located at the outer edge of the diabatic heating region, with an averaged  $Q_M = 4.6 \times 10^{-4} \text{ kgK}m^{-3}s^{-1}$ , which is about 60% of the selected  $M$  surfaces ( $Q_M = 7.6 \times 10^{-4} \text{ kgK}m^{-3}s^{-1}$ ). Because of this reason, the analyses in subsequent sections focus on the selected  $M$  surfaces that maximize  $Q_M$  and minimize  $RH_{deficit}$ .

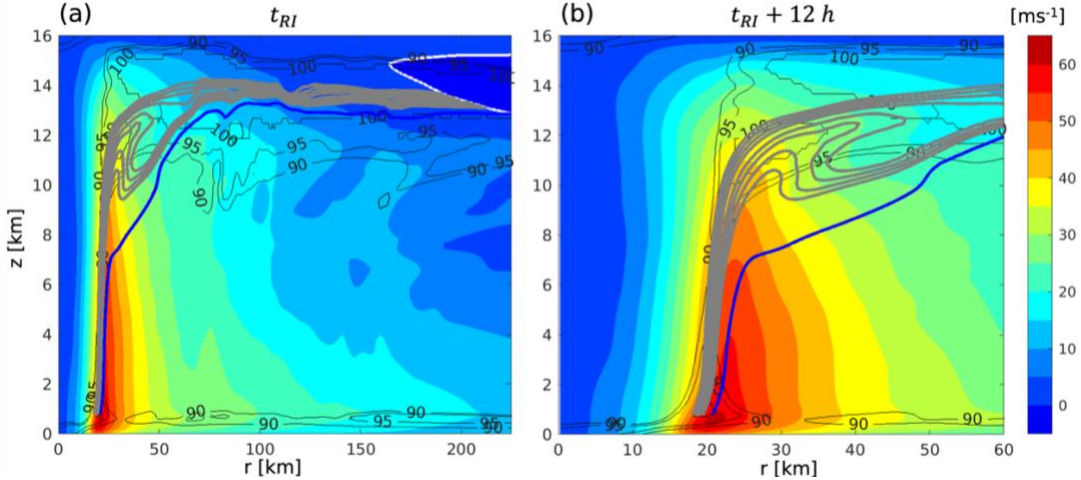


**Fig. 4:** Families of  $M$  surfaces of the CTRL experiment that satisfy the selection criteria (see text for details) at  $t_{RI}$ . Thin grey contours are relative humidity and white line denotes contour where  $v = 0 \text{ m s}^{-1}$ . (b) is similar to (a) but zooms in to display the details of the selected  $M$  surfaces at the eyewall region.

We now evaluate equation (13) within the intensification period, as shown in Fig. 5. The result shows that the all-term sum (red) shows nearly perfect agreement with the actual  $v_b$  throughout the entire intensification period. Importantly, previous studies showed that applying the traditional formula from PI (i.e.,  $\frac{v_b}{r_b} = -\frac{ds^*}{dM} (T_b - T_o)$ ) to the intensification period can result

in rather noisy data, particularly during the early stage of the intensification period (see Fig. 1 of Peng et al. 2018). Our current result from Fig. 5 not only confirms that the accuracy of equation (13), but it also shows that the generalized terms in equation (13) are the natural extension of previous PI formulations (Emanuel 1987 and Bryan and Rotunno 2009) into the Non-SN vortex regime, which is applicable to the entirety of the intensification period.

Among the terms, the bias-corrected balanced component is the dominant term that shows the largest increase during the intensification period. It is interesting to note that the bias term (magenta dashed line) is close to zero before  $t_{RI}$  but decreases to about  $-5 \text{ m s}^{-1}$  near the end of the intensification period, which can result in noticeable positive bias in the diagnosed  $v_m$  if the correction term is not included.

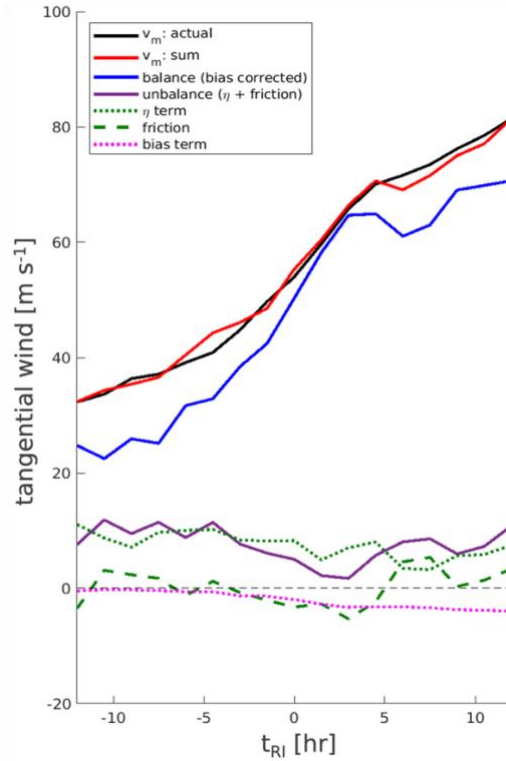


**Fig. 5:** Composite-mean time series for each term in equation 13. The actual  $v_m$  is shown in black. The solid purple line shows the unbalanced contribution, which is the sum of the  $\eta$  term (green dotted line) and frictional contribution (green dashed line).

On the other hand, the unbalanced term (sum of  $\eta$  term and frictional term) remains nearly constant during the intensification period. Peng et al. (2018) found that the tendency of the unbalanced term appears to supplement the difference in the intensification rate between the actual  $v_{max}$  and  $v_{EPI}$ , which contrasts with our current results. One possible reason is that our experiment uses a horizontal mixing length of 1500 m (default setting from CM1), while Peng et al. 2018 used

a rather small fixing length of 94 m, which can dramatically increase the supergradient component. With our current model setting, the result in Fig. 5 shows that the significant increase in  $v_{max}$  is largely attributed to the spin-up of the balanced vortex. Therefore, in the subsequent analyses, we only focus on examining the balanced term. We note here that even though the unbalanced term is small and largely uniform, it could potentially play important role in the intensification process (Smith et al. 2008), which will be examined further in future studies.

*c. Dependence of  $\left(\frac{\partial s^*}{\partial M}\right)_T$  on temperature*

Equation (13) shows that for a Non-SN vortex, the dependence of  $\left(\frac{\partial s^*}{\partial M}\right)_T$  on  $T$  is important to the balanced tangential wind at  $z_b$ . In this section, we examine this dependence closely.

Several interesting structures of  $\left(\frac{\partial s^*}{\partial M}\right)_T$  emerge when we examine the composite-mean evolution of  $\left(\frac{\partial s^*}{\partial M}\right)_T$ , as shown in Fig. 6. First, at  $t_{RI}$ ,  $\left(\frac{\partial s^*}{\partial M}\right)_T$  shows a clear linear structure as a function of  $T$ , with large negative value near 210-240 K and decaying towards the low level (Fig. 6e). Consistent with previous studies (Peng et al. 2018, 2019), this linear structure of  $\left(\frac{\partial s^*}{\partial M}\right)_T$  confirms that the SN assumption is not valid during the early intensification period (including  $t_{RI}$ ), since  $\left(\frac{\partial s^*}{\partial M}\right)_T$  would otherwise be constant with respect to variation of  $T$  along a given  $M$  surface.

At  $t_{RI} + 3h$ , the large negative value of  $\left(\frac{\partial s^*}{\partial M}\right)_T$  descend towards lower levels near 240 K (Fig. 6f). This trend continues in the subsequent hours, and  $\left(\frac{\partial s^*}{\partial M}\right)_T$  becomes more uniform in the mid-troposphere near 220 K - 260 K (Fig. 6g-i), indicating the vortex in the free troposphere becomes more symmetric neutral at this late stage, which agrees with E12 and Peng et al. (2018), (2019).

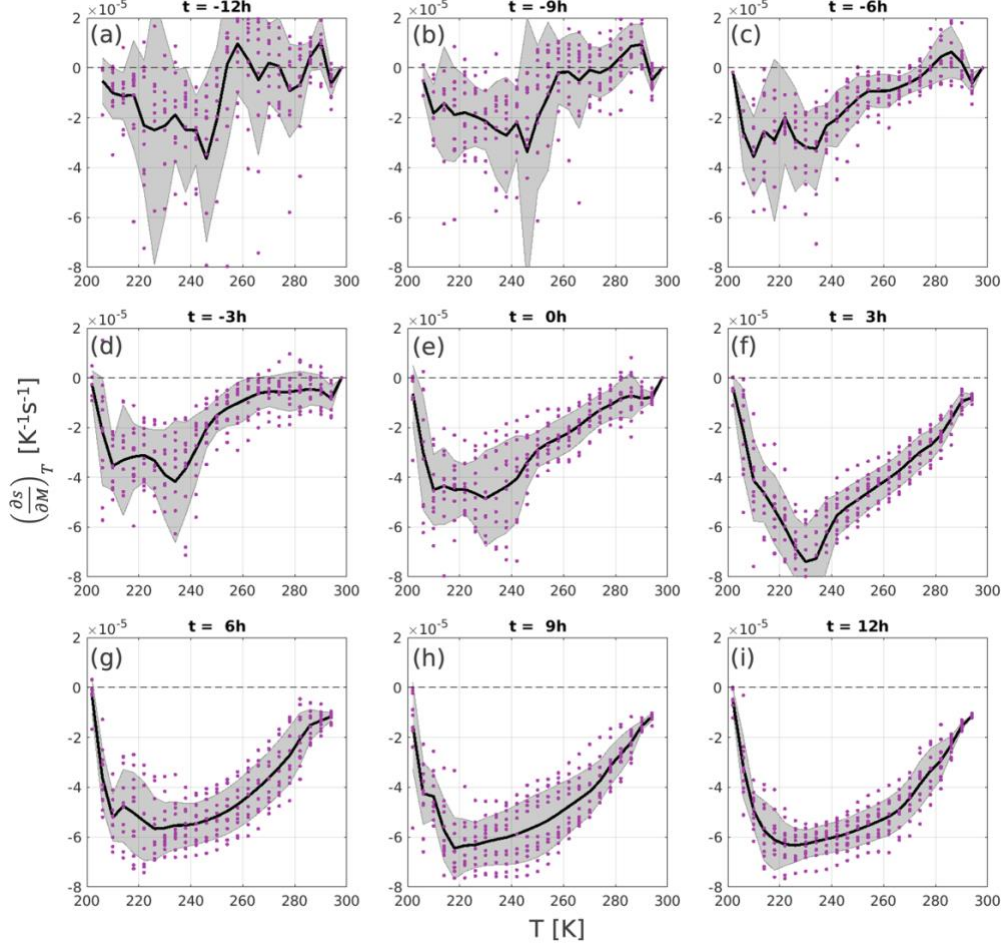


**Fig. 6:** Profiles of  $\left(\frac{\partial s^*}{\partial M}\right)_T$  as a function of  $T$  at every three hours during the intensification time window. The Black lines are the composite mean profile with shaded region indicate  $\pm 1$  standard deviation. The data points of each member are shown by the purple dots.

Another important and interesting feature emerges when compositing the mean  $\left(\frac{\partial s^*}{\partial M}\right)_T$  profiles during the intensification period, as shown in Fig. 7a. Near  $t_{RI} - 6 h$ ,  $\left(\frac{\partial s^*}{\partial M}\right)_T$  begins to develop large negative value near 210-240 K, which later further strengthens to  $-4 \times 10^{-5} K^{-1} s^{-1}$  at  $t_{RI}$ . This top-heavy profile of  $\left(\frac{\partial s^*}{\partial M}\right)_T$  between  $t_{RI} - 6 h$  to  $t_{RI}$  implies the development of a deep tall vortex that reaches tropopause, where the majority of the inward bending of  $M$  surfaces occur at the upper troposphere near 210-240 K. This structure suggests that the development a deep tall vortex preconditions the onset of maximum intensification rate, which is supported by the recent observational evidence on the relationship between vortex depth and intensification onset (Fischer et al. 2022, 2025; DesRosiers, et al. 2023).

At steady state after  $t = 8$  days (Fig. 7b),  $\left(\frac{\partial s^*}{\partial M}\right)_T$  indeed becomes nearly uniform at  $-6 \times 10^{-5} K^{-1}s^{-1}$  throughout the troposphere, while the boundary layer ( $T > 280 K$ ) shows noticeable gradient. This result confirms that symmetric neutrality is indeed a good approximation for steady-state TCs above the boundary layer. It is interesting to see that at steady state, the  $M$  surfaces reach the potential radius at a temperature of about 208 K, which is higher than the outflow temperature during the intensification period. This could potentially be due to the self-stratification process examined in ER11.

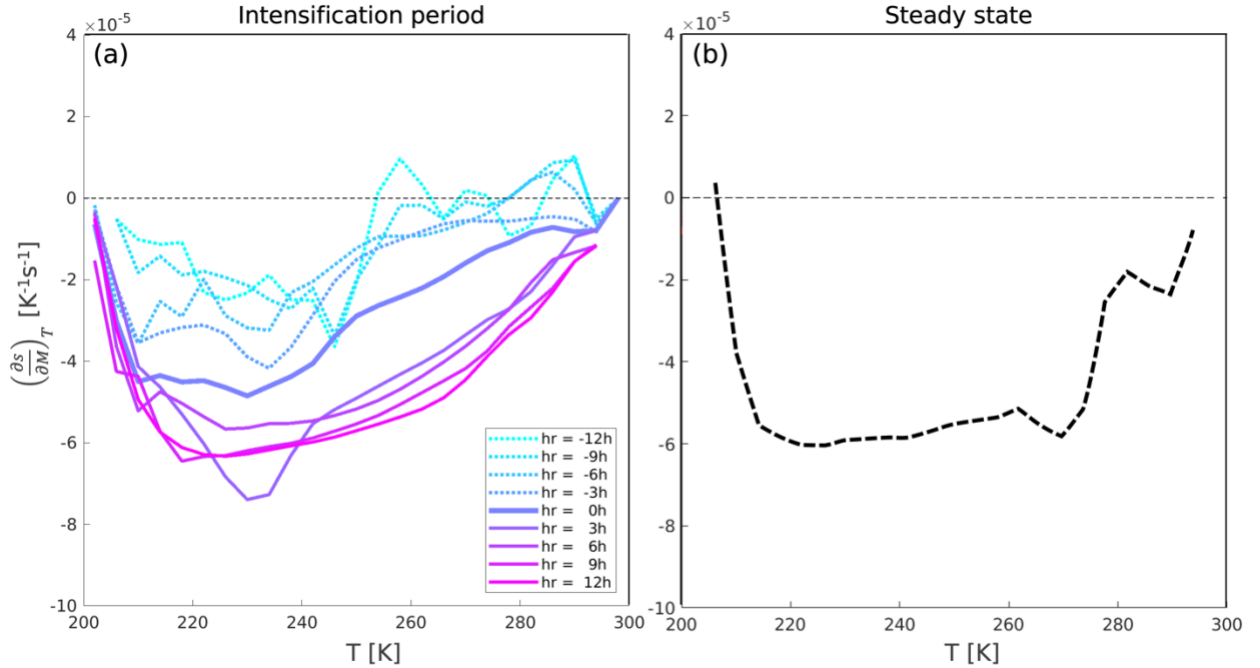


**Fig.7:** (a) Evolution of the composite mean profiles of  $\left(\frac{\partial s^*}{\partial M}\right)_T$  as a function of  $T$  at every three hours during the intensification time window. Profiles at  $t_{RI}$  (hr = 0 h) is thickened. (b) Similar to (a), but for steady state period during  $t = 192-198$  hour of the unperturbed member.

Why does  $\left(\frac{\partial s^*}{\partial M}\right)_T$  develop a large negative value near the tropopause, and what processes control its value there? First, we write  $\left(\frac{\partial s^*}{\partial M}\right)_T$  as  $\left(\frac{\partial s^*}{\partial M}\right)_T = \left(\frac{\partial s^*}{\partial M}\right)_p + \left(\frac{\partial s^*}{\partial p}\right)_M \left(\frac{\partial p}{\partial M}\right)_T$ . The second term is much smaller at the outflow region and  $\left(\frac{\partial s^*}{\partial M}\right)_T \approx \left(\frac{\partial s^*}{\partial M}\right)_p = \left(\frac{\partial s^*}{\partial r}\right)_p / \left(\frac{\partial M}{\partial r}\right)_p$ , which is proportional to baroclinicity divided by inertial stability. The cross-section of  $\left(\frac{\partial s^*}{\partial M}\right)_p$  (Fig. 8a) shows that large negative values of  $\left(\frac{\partial s^*}{\partial M}\right)_p$  exist between 205 K and 210 K, covering 30 and 60 km

radius. On the other hand,  $\left(\frac{\partial s^*}{\partial r}\right)_p$  shows large negative values within 40 km radius (Fig. 8b) and is not sufficient to explain the spatial structure of the negative  $\left(\frac{\partial s^*}{\partial M}\right)_p$ . In contrast, near 40-60 km,  $\left(\frac{\partial M}{\partial r}\right)_p^{-1}$  shows large value due to the decrease of  $\left(\frac{\partial M}{\partial r}\right)_p$  to small value (nearly zero) at these radii (Fig. 8c), resulting in the significant amplification of  $\left(\frac{\partial s^*}{\partial M}\right)_p$ . Therefore, the decrease of inertial stability is the major cause of the large negative values of  $\left(\frac{\partial s^*}{\partial M}\right)_T$  near 205-210 K.

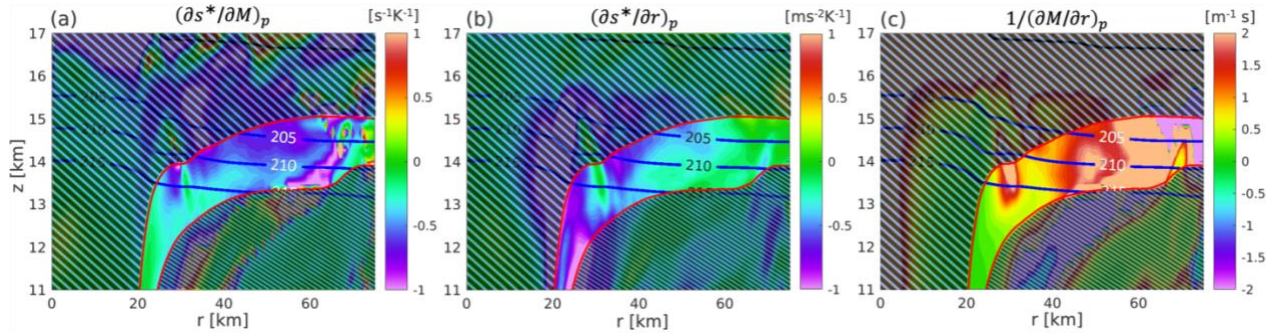


**Fig.8:** (a) Cross-sections of  $\left(\frac{\partial s^*}{\partial M}\right)_p$  normalized by  $10^{-4}$  of the unperturbed member at  $t = t_{RI}$ . The regions outside the smallest and largest  $M$  surfaces (red contours) are hatched. Blue contours indicate temperature contours of 205, 210 and 215 K. (b) and (c) are the same as (a), but for cross-sections of  $\left(\frac{\partial s^*}{\partial r}\right)_p$  and  $\left(\frac{\partial M}{\partial r}\right)_p^{-1}$ , respectively.

The decrease of  $\left(\frac{\partial M}{\partial r}\right)_p$  to small value can be understood using the conservation principle of moist potential vorticity (PV),  $P_e \equiv \frac{1}{r} \frac{(\nabla M \times \nabla \theta_e) \cdot \hat{\lambda}}{\rho}$ . In the free troposphere of an axisymmetric flow where the forcing of angular momentum and moist entropy are small (assuming reversible moist process),  $P_e$  is approximately conserved due to vanishing the baroclinic term under axisymmetric or saturation condition<sup>3</sup> (both satisfied in the present case). Before SN is valid, the moist PV at the low-level eyewall region is dominantly negative, owing to the positive vertical vorticity and decrease of  $\theta_e$  with height (i.e., convective instability). As the parcels rise to the outflow region at the upper troposphere,  $\theta_e$  converges to  $\theta$  and increases vertically due to the lack

<sup>3</sup> Schubert et al. (2001) showed that the baroclinic term  $\frac{1}{\rho^3} \nabla \theta_e \cdot (\nabla \rho \times \nabla p)$  does not vanish if  $\theta_e$  is used to define PV. However, the baroclinic term indeed vanishes if the flow is either saturated or axisymmetric. If the air is saturated,  $\theta_e$  becomes  $\theta_{es}$  and is approximately only a function of  $\rho$  and  $p$  and thus  $\nabla \theta_e \cdot (\nabla \rho \times \nabla p) = 0$ . For axisymmetric flow,  $\nabla \rho \times \nabla p$  points at the azimuthal direction, while  $\nabla \theta_e$  lies in the radius-height plane, so  $\nabla \theta_e \cdot (\nabla \rho \times \nabla p)$  also vanishes.

of moisture at the upper troposphere. To conserve the negative moist PV, the parcel's vertical vorticity (and dry PV,  $P \equiv \frac{1}{r} \frac{(\nabla M \times \nabla \theta) \cdot \hat{\lambda}}{\rho}$ ) must change sign from positive to negative along the ascending path. Describing the flow in terms of dry PV, i.e.,  $\frac{DP}{Dt} = \frac{\zeta_a \cdot \nabla \dot{\theta}}{\rho}$ , we see that the sign change of dry PV is due to the eyewall diabatic heating ( $\dot{\theta}$ ). Since  $\dot{\theta}$  is spatially correlated with vertical motion  $w$ , this dry PV forcing causes negative tilting, which results in negative vorticity and a widespread region of small  $\left(\frac{\partial M}{\partial r}\right)_p$  values near the outflow region.

The above discussion explains the development of large negative values of  $\left(\frac{\partial s^*}{\partial M}\right)_p$  near the tropopause, but not the precise value there. To answer this question, we can use the angular momentum and entropy equations. In pressure coordinate, we write the secondary circulation in terms of nondivergent streamfunction, i.e.,  $u = -\frac{1}{r} \frac{\partial \psi}{\partial p}$  and  $\omega = \frac{1}{r} \frac{\partial \psi}{\partial r}$ . Taking time averaging of 3 hours and separating the nonlinear advection terms into mean and transient eddy contributions, the conservation principles of  $M$  and  $s^*$  can be written as

$$\frac{\delta M}{\delta t} + \overline{\frac{1}{r} \frac{\partial \psi}{\partial z} \left(\frac{\partial \bar{M}}{\partial r}\right)}_{\psi} + \overline{\left(\frac{1}{r} \frac{\partial \psi}{\partial z}\right)' \left(\frac{\partial M}{\partial r}\right)'}_{\psi} = \overline{F_M} \quad (19a)$$

$$\frac{\delta s^*}{\delta t} + \overline{\frac{1}{r} \frac{\partial \psi}{\partial z} \left(\frac{\partial \bar{s}^*}{\partial r}\right)}_{\psi} + \overline{\left(\frac{1}{r} \frac{\partial \psi}{\partial z}\right)' \left(\frac{\partial s^*}{\partial r}\right)'}_{\psi} = \overline{F_{s^*}} \quad (19b)$$

where overbar denotes 3-hourly time means; the (') terms denote temporal perturbations from the 3-hourly time mean; and  $\delta$  denotes the change in the 3-hour time interval. The first tendency terms in (19a,b) are at least one order smaller than the rest terms and can be neglected. Rearranging the terms and dividing the two equations then yield

$$\left(\frac{\partial \bar{s}^*}{\partial \bar{M}}\right)_{\psi} \approx \frac{\overline{F_{s^*}} + F_{s^*,eddy}}{\overline{F_M} + F_{M,eddy}}; \quad (20)$$

$$F_{s^*,eddy} = -\overline{\left(\frac{1}{r} \frac{\partial \psi}{\partial z}\right)' \left(\frac{\partial s^*}{\partial r}\right)'}_{\psi}; \quad F_{M,eddy} = -\overline{\left(\frac{1}{r} \frac{\partial \psi}{\partial z}\right)' \left(\frac{\partial M}{\partial r}\right)'}_{\psi}$$

The eddy forcing terms ( $F_{s^*,eddy}$  and  $F_{M,eddy}$ ) represent the time-mean effects of the resolved nonlinear advection of  $s^*$  and  $M$  by the transient eddies. As the secondary circulation reach the

tropopause, a large portion of isolines of streamfunction spread outward and become nearly parallel to temperature contours, and thus  $\left(\frac{\partial \bar{s}^*}{\partial \bar{M}}\right)_\psi \approx \left(\frac{\partial \bar{s}^*}{\partial \bar{M}}\right)_T$  and

$$\left(\frac{\partial \bar{s}^*}{\partial \bar{M}}\right)_T \approx \frac{\bar{F}_{s^*} + F_{s^*,eddy}}{\bar{F}_M + F_{M,eddy}} \quad (21)$$

Fig. 9 shows the scattered plot of  $\left(\frac{\partial \bar{s}^*}{\partial \bar{M}}\right)_\psi$  against  $\left(\frac{\partial \bar{s}^*}{\partial \bar{M}}\right)_T$  at  $t_{RI}$  of all experiments near the outflow region. All data points fall near the diagonal line, with a mean value around  $-5.5 \times 10^{-5} [K^{-1}s^{-1}]$ . The good agreement between the two variables confirms that  $\left(\frac{\partial \bar{s}^*}{\partial \bar{M}}\right)_T$  near tropopause is controlled by the ratio of total entropy forcing to total momentum forcing at the outflow region. We note here that while the strong mixing near the outflow determines the precise value of  $\left(\frac{\partial \bar{s}^*}{\partial \bar{M}}\right)_T$ , the root cause of this mixing stems from the development of an inertially unstable region near the outflow region, as explained previous paragraph.

Peng et al. (2019) show that as the eyewall updrafts reach tropopause, there is a bias for the parcels to develop into outflow due to internal gravity wave generation and propagation. Our results presented herein similarly indicate that the development of transient eddies (deviation from 3-hourly time mean), which include internal gravity waves, can contribute to the mixing of  $s^*$  and  $M$ . Together with subgrid-scale turbulent mixing, they modulate the value of  $\left(\frac{\partial \bar{s}^*}{\partial \bar{M}}\right)_T$  near the tropopause, constraining the structure of  $M$  surfaces at the upper-level outflow region.

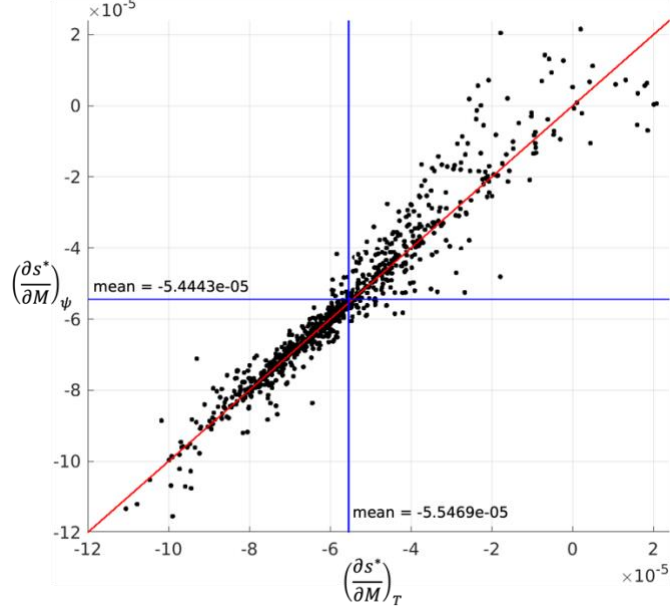


**Fig.9:** Scattered plot of  $\left(\frac{\partial s^*}{\partial M}\right)_\psi$  versus  $\left(\frac{\partial s^*}{\partial M}\right)_T$  of all members at  $t_{RI}$ . The data points are collected near the outflow region, with  $r$  between 30 and 80 km radii and  $z$  between 13.5 and 15 km. We exclude grid points where the normalized Jacobians  $\frac{|J(M,T)|}{|\nabla M||\nabla T|}$  or  $\frac{|J(M,\psi)|}{|\nabla M||\nabla \psi|}$  are less than 0.01 to avoid data near singularities of  $\left(\frac{\partial s^*}{\partial M}\right)_\psi$  and  $\left(\frac{\partial s^*}{\partial M}\right)_T$ .

## 5. Discussion

### a. On the computation of $\frac{\partial s^*}{\partial M}$ and associated uncertainty

Equation (9) shows that for non-SN vortex, it is the *gradient between  $s^*$  and  $M$  along constant temperature*, i.e.,  $\left(\frac{\partial s^*}{\partial M}\right)_T$ , that constrains the slope of the inward bending  $M$  surfaces of a balanced vortex. One thing that needs to be highlighted is that if one does not specify the direction in which  $\frac{\partial s^*}{\partial M}$  is evaluated, the magnitude of  $\frac{\partial s^*}{\partial M}$  can be *highly variable and uncertain*. As shown in Fig. 10a, if the  $\frac{\partial s^*}{\partial M}$  is evaluated along constant  $s^*$  direction, then  $\left|\left(\frac{\partial s^*}{\partial M}\right)_{s^*}\right|$  is *identically zero*. If  $\frac{\partial s^*}{\partial M}$  is taken along constant  $M$  direction, then  $\left|\left(\frac{\partial s^*}{\partial M}\right)_M\right|$  is in fact  $+\infty$  (Fig. 10b)<sup>4</sup>. Thus, for a non-SN vortex, the magnitude of  $\frac{\partial s^*}{\partial M}$  can range anywhere between 0 and  $+\infty$  if the direction of derivative

<sup>4</sup> Except when under SN condition where  $s^*$  and  $M$  are congruent, both  $\left(\frac{\partial s^*}{\partial M}\right)_{s^*}$  and  $\left(\frac{\partial s^*}{\partial M}\right)_M$  become indeterminate, whose limits equal to  $\frac{ds^*}{dM}$ .

varies slightly. Therefore, we should be cautious about how  $\frac{\partial s^*}{\partial M}$  is computed when the SN condition is not valid. Importantly, our results presented herein proved that *among all possible directions*, it is the gradient along *constant temperature* that imposes physical constraints on the vortex structure consistent with balanced dynamics (Fig. 10c).

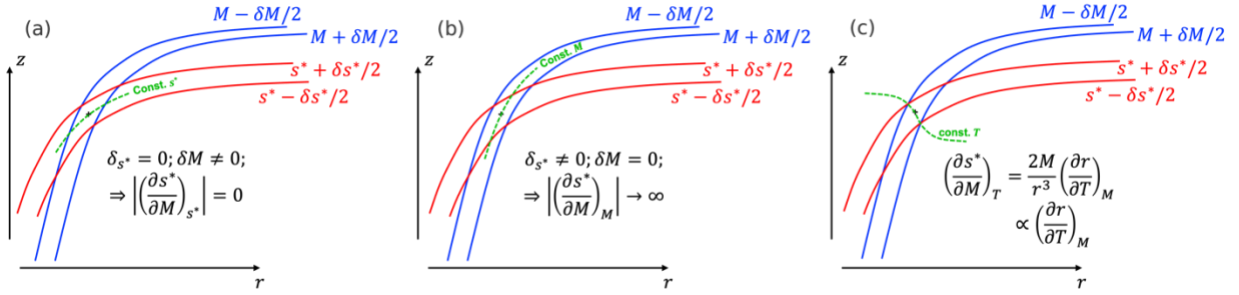


**Fig. 10:** Schematics illustrating the differences of partial derivative of  $s^*$  w.r.t  $M$  along different directions: (a) along  $s^*$  isoline; (b) along  $M$  isoline; and (c) along  $T$  isoline. The direction where the derivative is held constant is shown by the green dashed line.

*b. Issues of the time-dependent intensification model of Wang et al. 2021b*

Wang et al. 2021b (W21b) developed a time-dependent intensification model that includes an ad-hoc parameter  $A'$  to represent the effects of non-SN vortex structure on the TC intensification rate. It is, therefore, necessary to examine whether their findings are consistent with our generalized results. Specifically, equation (14) of W21b can be arranged as

$$M_{h,r_m} \left( \frac{1}{r_m^2} - \frac{1}{r_o^2} \right) = -A' \left. \frac{\partial s^*}{\partial M} \right|_{h,r_m} (T_b - T_o) \quad (22)$$

, where  $\left. \frac{\partial s^*}{\partial M} \right|_{h,r_m}$  and  $M_{h,r_m}$  are  $\frac{\partial s^*}{\partial M}$  and  $M$  evaluated at the boundary layer top ( $z = h$ ) and at the

radius of maximum wind ( $r_m$ ). Note that  $M_{h,r_m} \left( \frac{1}{r_m^2} - \frac{1}{r_o^2} \right) = \left( \frac{r_m v_m + \frac{1}{2} f r_m^2}{r_m^2} - \frac{\frac{1}{2} f r_o^2}{r_o^2} \right) = \frac{v_m}{r_m}$  and that

$\frac{v_m}{r_m} = \int_{T_b}^{T_o} \left( \frac{\partial s^*}{\partial M} \right)_T dT$  as proven in our equation (9). We note here that the derivation of W21b

follows the balanced framework of E86 and that  $A'$  is supposed to capture the effect of the non-SN vortex on the balanced intensity. While W21b did not specify clearly along what direction they evaluate  $\frac{\partial s^*}{\partial M}$  at  $(r_m, h)$ , let us first assume that their treatment is consistent with balanced dynamics

and evaluate  $\left. \frac{\partial s^*}{\partial M} \right|_{h,r_m}$  as  $\left( \frac{\partial s^*}{\partial M} \right)_T \Big|_{h,r_m}$ . Rearranging equation (22) as below

$$A' = \frac{\frac{1}{T_o - T_b} \int_{T_b}^{T_o} \left( \frac{\partial s^*}{\partial M} \right)_T dT}{\left( \frac{\partial s^*}{\partial M} \right)_T \Big|_{h,r_m}} = \frac{\overline{\left( \frac{\partial s^*}{\partial M} \right)_T}}{\left( \frac{\partial s^*}{\partial M} \right)_T \Big|_{h,r_m}} \quad (23)$$

, where  $\overline{\left( \frac{\partial s^*}{\partial M} \right)_T} \equiv \frac{1}{T_o - T_b} \int_{T_b}^{T_o} \left( \frac{\partial s^*}{\partial M} \right)_T dT$ , we see that  $A'$  is precisely the ratio of the averaged  $\left( \frac{\partial s^*}{\partial M} \right)_T$  between  $T_b$  and  $T_o$  to the value of  $\left( \frac{\partial s^*}{\partial M} \right)_T \Big|_{h,r_m}$  at the boundary layer top. W21b assumed  $0 \leq A' \leq 1$ , which, from equation (23), is equivalent to assuming  $\left| \overline{\left( \frac{\partial s^*}{\partial M} \right)_T} \right| \leq \left| \left( \frac{\partial s^*}{\partial M} \right)_T \Big|_{h,r_m} \right|$ . However, from Fig. 7a,  $\left( \frac{\partial s^*}{\partial M} \right)_T$  clearly develops a top-heavy structure throughout the intensification period, so it is apparent that  $\left| \overline{\left( \frac{\partial s^*}{\partial M} \right)_T} \right| > \left| \left( \frac{\partial s^*}{\partial M} \right)_T \Big|_{h,r_m} \right|$  and  $A' > 1$  in our experiment, which does not agree with the *assumption of W21b and their experimental data*.

This discrepancy mainly arises due to how W21b evaluated  $\frac{\partial s^*}{\partial M}$  in their experiments. A recent follow-up study by the authors (Li et al. 2024, their appendix B) revealed that W21b evaluated  $\frac{\partial s^*}{\partial M} \Big|_{h,r_m}$  along the direction *perpendicular to  $s^*$  contour* ( $\perp s^*$ ), i.e.,  $\left( \frac{\partial s^*}{\partial M} \right)_{\perp s^*} \Big|_{h,r_m}$ . However, Li et al. (2024) and W21b did not provide any physical justification for such a choice of evaluation direction. For a non-SN vortex where  $s^*$  field has not fully developed a vertically connected structure,  $\perp s^*$  direction would have a large vertical component (Fig. 11, also see Fig. B1 of Li et al. 2024), which is clearly inconsistent with  $\left( \frac{\partial s^*}{\partial M} \right)_T$  and balanced dynamics.

If the evaluation of  $A'$  in W21b is inconsistent with balanced dynamics, then what does  $A'$  in W21b represent? W21b used the slab boundary layer equations of  $s^*$  and  $M$  that do not contain vertical advection terms (their equations 5 and 6). For non-SN vortex<sup>5</sup>, neglecting vertical advection near the eyewall region is unjustified and perhaps *unnecessary*. Assuming enelastic approximation and writing  $(u, w)$  as  $\left( \frac{1}{r\rho} \frac{\partial \psi}{\partial z}, -\frac{1}{r\rho} \frac{\partial \psi}{\partial r} \right)$ , the total advection can be written as  $u \frac{\partial \alpha}{\partial r} + w \frac{\partial \alpha}{\partial z} = u \left( \frac{\partial \alpha}{\partial r} + \frac{\partial \alpha}{\partial z} \left( \frac{\partial z}{\partial r} \right)_\psi \right) = u \left( \frac{\partial \alpha}{\partial r} \right)_\psi$ , where  $\alpha$  can be any scalar. Continuing their

---

<sup>5</sup> If SN assumption is made and  $M$  is used as horizontal coordinate, then vertical advection may be neglected since the eyewall is water saturated and  $\left( \frac{\partial s^*}{\partial p} \right)_M = 0$ , as in E12. However, these conditions are not satisfied in W21b.

derivation, we see that the  $\frac{\partial s^*}{\partial M}$  term would emerge as  $\left(\frac{\partial s^*}{\partial r}\right)_\psi / \left(\frac{\partial M}{\partial r}\right)_\psi = \left(\frac{\partial s^*}{\partial M}\right)_\psi$  in equation (8) of W21b. For a non-SN vortex during intensification,  $\psi$  contours must cross both  $M$  and  $s^*$  (thus project onto  $\perp s^*$  direction) to evolve both fields. Therefore, this indicates that evaluating  $A'$  using  $\left(\frac{\partial s^*}{\partial M}\right)_{\perp s^*}$  should bear similar physical meaning as  $\left(\frac{\partial s^*}{\partial M}\right)_\psi$ , and thus effectively parameterizing *the ratio of total advection of  $s^*$  to that of  $M$  within the TC boundary layer*, which is an unbalanced nonlinear process, rather than the balanced dynamics of the non-SN vortex.

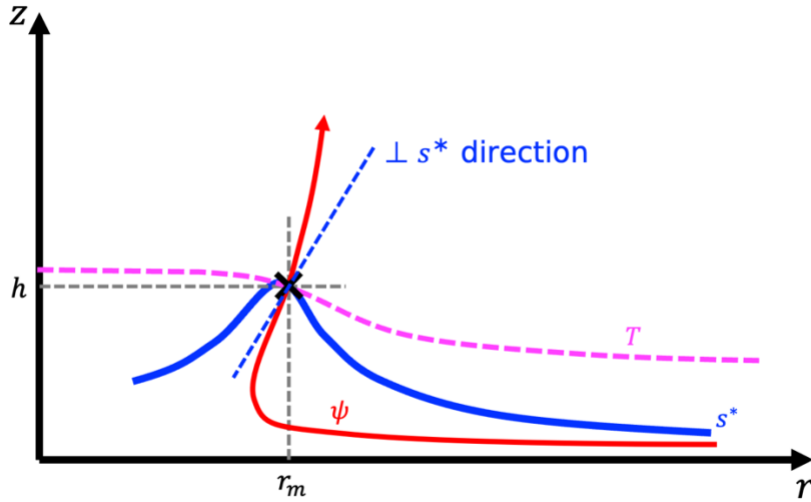


**Fig. 11:** Schematics illustrating the structure of saturation entropy  $s^*$  (solid blue), temperature  $T$  (dashed magenta), and nondivergent streamfunction  $\psi$  (solid red, with arrow denoting flow direction) of a non-SN vortex. Grey dashed lines and the black cross indicate the radius of maximum wind  $r_m$  at the boundary layer top  $z = h$ . Blue dashed line denotes direction perpendicular to the  $s^*$  contour, which projects strongly into vertical direction and does not align with constant  $T$  direction.

The above discussion highlights the fact that computing  $\frac{\partial s^*}{\partial M}$  without specifying the direction of evaluation can lead to rather misleading interpretations. In addition, while the approach of ad hoc parameters can yield results that seemingly match numerical model simulations, its shortcomings are also apparent: the dynamics are buried in the dependence of those ad hoc parameters, making it challenging to discern the underlying physics. Furthermore, it is difficult to ensure that the dependence of these parameters can be generalized to scenarios beyond the set of experiments used to determine their values.

## 6. Conclusion

In this study, the potential intensity theory (PI, Emanuel 1986, Emanuel and Rotunno 2011, Bryan and Rotunno 2009) is revisited without making the symmetric neutrality (SN) assumption, with the goal of uncovering the saturated vortex dynamics before the SN assumption is valid.

Several important findings are identified by relaxing the SN assumption. First, it is found that saturated balanced vortex dynamics constrain the curved structure of an absolute angular momentum  $M$  isoline through establishing a local gradient between saturation entropy  $s^*$  and  $M$  along the direction of constant temperature  $T$ , i.e.,  $\left(\frac{\partial s^*}{\partial M}\right)_T$ . This constraint is sufficient to determine the balanced intensity at the low level, i.e.,  $\frac{v_m}{r_m} = \int_{T_b}^{T_o} \left(\frac{\partial s^*}{\partial M}\right)_T dT$ . This finding can be modified to show that a saturated TC eyewall with an intense (balanced) wind field at the low level is a circular frontal zone of integrated saturation entropy.

By incorporating the radial and vertical momentum advection and momentum forcings, we obtain generalized unbalanced terms that converge to the supergradient wind component derived by Bryan and Rotunno (2009a). The relaxation of the SN assumption also allows us to obtain additional terms that represent contributions from radial and vertical momentum forcing. All these terms combined to form the generalized  $v_{max}$  formula that applies to within the TC boundary layer before the SN assumption is valid.

An ensemble of axisymmetric numerical simulations is conducted to verify the validity of the generalized  $v_{max}$  formula. The results show that this generalized formula can accurately quantify the contributions of the various processes during the intensification period, demonstrating that it is the natural extension of the traditional PI (balanced and/or unbalanced)  $v_{max}$  formula into the non-SN regime.

Focusing on the 24 hours centered at the time of maximum intensification rate, several interesting findings regarding the balanced component are revealed. Before the intensification rate reaches peak value,  $\left(\frac{\partial s^*}{\partial M}\right)_T$  within the saturated eyewall first develops a top-heavy, linear structure as a function of temperature, with large negative value occurring at the upper troposphere near temperature of 210-240 K. This linear dependence on temperature confirms that SN assumption is not valid at the time of peak intensification rate. The top-heavy structure of  $\left(\frac{\partial s^*}{\partial M}\right)_T$  during the early phase of intensification suggests that the development of a deep tall vortex is potentially important

to the onset of intensification process, consistent with recent observational evidence (Fischer et al. 2022, 2025; DesRosiers, et al. 2023). Further examination of the outflow region shows that the large negative  $\left(\frac{\partial s^*}{\partial M}\right)_T$  value is amplified by the inertial instability at the outflow region, with precise value controlled by the ratio of entropy forcing to momentum forcing (mixing due to transient eddies). These results indicate the importance of resolved and parameterized mixing in controlling the inward bending structure of  $M$  surfaces at the tropopause outflow region, consistent with Emanuel (2012).

The theoretical results identified in the study have other important implications. First, the generalized balanced  $v_{max}$  component shows that the distribution of saturation entropy along  $M$  surfaces directly determines the balanced  $v_{max}$  at the low level (equations 9, 10), thus providing an explicit linkage for investigating the impacts of ventilation on TC intensity under non-SN conditions. Second, it is found that tropopause mixing determines the overall vertical gradient of  $\left(\frac{\partial s^*}{\partial M}\right)_T$  in the free troposphere, thus modulating the magnitude and potential roles of vertical advection of entropy in the intensification process, an effect neglected by previous studies due to the SN assumption.

Because the goal of this study is to derive and explore the detailed vortex dynamics in the non-SN regime, many aspects of the results cannot be covered due to the length of the manuscript. These include examination of the unbalanced contributions of the  $v_{max}$  formula and their sensitivity to experimental parameters such as horizontal mixing length. The sensitivity of our findings on the ratio of drag and enthalpy exchange coefficients is also an interesting topic that needs to be further explored.

### **Acknowledgments**

I thank Drs. Richard Rotunno, Kerry Emanuel, Brian Tang, Robert Fovell, Bolei Yang, Daniel Chavas and Chris Davis for their insightful discussion and encouragement. I also greatly appreciate the three anonymous reviewers for the careful and detailed reviews, which provided immensely valuable feedbacks to improve the clarity and correctness of the major findings of this work.

### **Data availability statement**

The CM1 namelist files and model output are available upon request via a University at Albany Thematic Real-time Environmental Distributed Data Services (THREDDS) server.

## Appendix A: Five equivalent forms of a Jacobian Matrix Determinant

In this appendix, I document the derivation of a few equivalent Jacobian forms used to derive some of the major findings of this study.

Let  $J$  be the Jacobian matrix determinant of a two-dimensional transformation from  $(M, p)$  space to  $(s^*, T)$  space, defined as

$$\begin{aligned} J\left(\frac{s^*, T}{M, p}\right) &:= \det \begin{pmatrix} \frac{\partial s^*}{\partial M} & \frac{\partial s^*}{\partial p} \\ \frac{\partial T}{\partial M} & \frac{\partial T}{\partial p} \end{pmatrix} \\ &= \left(\frac{\partial T}{\partial p}\right)_M \left(\frac{\partial s^*}{\partial M}\right)_p - \left(\frac{\partial T}{\partial M}\right)_p \left(\frac{\partial s^*}{\partial p}\right)_M \end{aligned} \quad (\text{A1})$$

If we factor out  $\left(\frac{\partial s^*}{\partial M}\right)_p$  in (A.1), we can then use the triple product rule of partial derivatives

$$\begin{aligned} \left(\frac{\partial s^*}{\partial p}\right)_M \left(\frac{\partial M}{\partial s^*}\right)_p \left(\frac{\partial p}{\partial M}\right)_{s^*} &= -1 \text{ and the fact that } \left(\frac{\partial T}{\partial p}\right)_{s^*} = \left(\frac{\partial T}{\partial p}\right)_M + \left(\frac{\partial T}{\partial M}\right)_p \left(\frac{\partial M}{\partial p}\right)_{s^*} \text{ to rewrite } J\left(\frac{s^*, T}{M, p}\right) \\ J\left(\frac{s^*, T}{M, p}\right) &= \left(\frac{\partial s^*}{\partial M}\right)_p \left( \left(\frac{\partial T}{\partial p}\right)_M + \left(\frac{\partial T}{\partial M}\right)_p \left(\frac{\partial M}{\partial p}\right)_{s^*} \right) = \left(\frac{\partial s^*}{\partial M}\right)_p \left(\frac{\partial T}{\partial p}\right)_{s^*} \end{aligned} \quad (\text{A2})$$

Following the same procedure and factoring the other three partial derivatives of (A.1), we show that  $J\left(\frac{s^*, T}{M, p}\right)$  may be written in at least four alternative equivalent ways:

$$J\left(\frac{s^*, T}{M, p}\right) = \left(\frac{\partial T}{\partial p}\right)_M \left(\frac{\partial s^*}{\partial M}\right)_p - \left(\frac{\partial T}{\partial M}\right)_p \left(\frac{\partial s^*}{\partial p}\right)_M = \left(\frac{\partial T}{\partial p}\right)_{s^*} \left(\frac{\partial s^*}{\partial M}\right)_p \quad (\text{A3a})$$

$$= \left(\frac{\partial T}{\partial p}\right)_M \left(\frac{\partial s^*}{\partial M}\right)_T \quad (\text{A3b})$$

$$= -\left(\frac{\partial s^*}{\partial p}\right)_M \left(\frac{\partial T}{\partial M}\right)_{s^*} \quad (\text{A3c})$$

$$= -\left(\frac{\partial T}{\partial M}\right)_p \left(\frac{\partial s^*}{\partial p}\right)_T \quad (\text{A3d})$$

Each of (A.3a)-(A.3d) represents a specific order of transformation from  $(M, p)$  to  $(T, s)$  spaces, as shown in Figure A1; while (A.1) only specifies the start- and end-point of the transformation. Note that the Jacobian for transformation from  $(s^*, T)$  to  $(T, s^*)$  is -1, meaning that the dimensional order of the coordinate system matters (Fig. A1b).

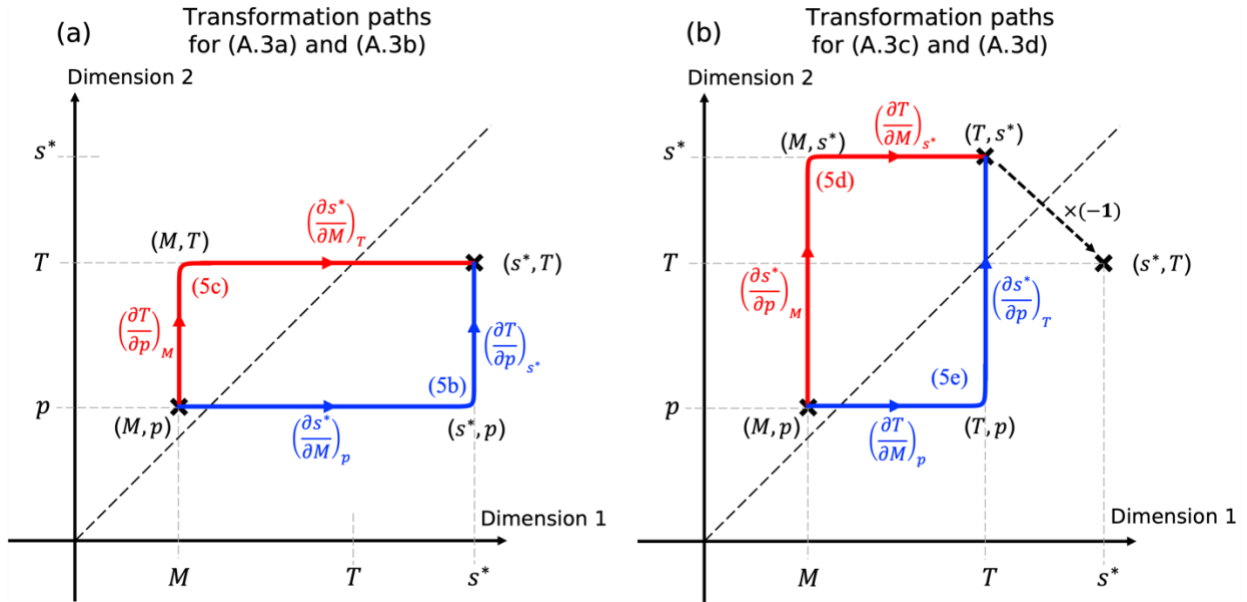


**Fig.A1:** (a) A schematic illustrating the transformation paths from  $(M, p)$  space to  $(s^*, T)$  space based on equations A.3a (blue) and A.3b (red). The Jacobian determinant for each transformation step is shown next to the transformation path. The horizontal and vertical axes represent all possible coordinate variables; each point in the two-dimensional space is a unique coordinate system. (b) is similar to (a), but for equations A.3c (red) and A.3d (blue). The thick black dashed arrow represents the transformation from  $(T, s^*)$  to  $(s^*, T)$  space, which has a Jacobian determinant of  $-1$ .

## Appendix B: Derivation of balanced tangential wind using the energetic balance (5)

The balanced tangential wind shown in equation (9) was derived using one of the Jacobian forms (A.3b). In this appendix, we derive (9) and (10) based on the energetic property (5), i.e.,

$$dM^2 d\left(-\frac{1}{2r^2}\right) = ds^* dT.$$

For a given  $M$  surface ( $M_0$ ) within the saturated eyewall region, without loss of generality, we consider the narrow region bounded by the two adjacent  $M$  surfaces surrounding  $M_0$  (i.e.,  $M_{-1} = M_0 - \frac{\delta M}{2}$  and  $M_1 = M_0 + \frac{\delta M}{2}$ , with infinitesimal  $\delta M$ ) and the two *constant* temperature surfaces  $T_b$  and  $T_o$ , as shown in Fig. B1a. Here,  $T_o$  is the temperature at the outflow radius  $r_o$  where  $v$  at the  $M_0$  surface becomes 0. Because  $M$  is the vertical axis in  $(-1/2r^2, M^2)$  space and that  $\delta M$  is infinitesimal, the region of interest in  $(-1/2r^2, M^2)$  space is an infinitesimally shallow trapezoid (Fig. B1b), with thickness  $M_1^2 - M_{-1}^2 \approx 2M_0\delta M$ . To the first order of  $\delta M$ , the area of this region can be computed as a shallow parallelogram of width  $\left(-\frac{1}{2r_o^2} + \frac{1}{2r_b^2}\right)$ .

$$Area_{(M^2, -1/2r^2)} = 2M_0\delta M \times \left(-\frac{1}{2r_o^2} + \frac{1}{2r_b^2}\right) \quad (\text{B1})$$

Because  $M_0 = \frac{1}{2}fr_o^2 = r_b v_b + \frac{1}{2}fr_b^2$ ,  $Area_{(M^2, -1/2r^2)} = \delta M \times \left(-\frac{2M_0}{2r_o^2} + \frac{2M_0}{2r_b^2}\right) = \frac{v_b}{r_b} \delta M$ .

On the other hand, the structure of the same region in  $(s^*, T)$  space depends on the shape of the  $M_1$  and  $M_2$  isolines in  $(s^*, T)$  space, as shown in Fig. B1c. To calculate the area, the first approach would be to discretize the region into thin layers of infinitesimal thickness  $\delta T$ . The width  $\delta s^*$  of each layer can be computed as  $\left(\frac{\partial s^*}{\partial M}\right)_T \delta M$ . Therefore,  $Area_{(s^*, T)}$  can be computed as

$$Area_{(s^*, T)} = \sum_i \left(\frac{\partial s^*}{\partial M}\right)_T \delta M \delta T = \delta M \sum_i \left(\frac{\partial s^*}{\partial M}\right)_T \delta T \quad (\text{B2})$$

Taking  $\delta T \rightarrow 0$ ,  $\delta M \sum_i \left(\frac{\partial s^*}{\partial M}\right)_T \delta T$  becomes  $\delta M \int_{T_b}^{T_o} \left(\frac{\partial s^*}{\partial M}\right)_T dT$ . By the energetic property (5), we have  $\frac{v_b}{r_b} \delta M = \delta M \int_{T_b}^{T_o} \left(\frac{\partial s^*}{\partial M}\right)_T dT$ . Canceling  $\delta M$  yields

$$\frac{v_b}{r_b} = \int_{T_b}^{T_o} \left(\frac{\partial s^*}{\partial M}\right)_T dT \quad (\text{B3})$$

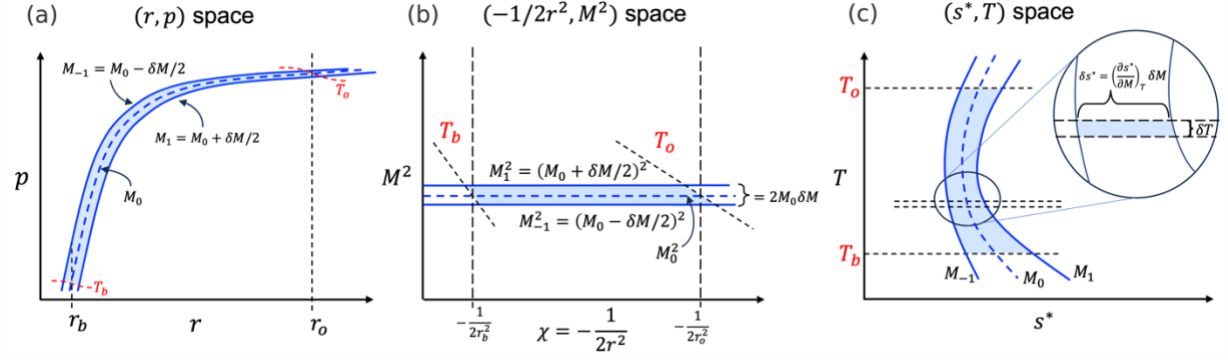


**Fig. B1:** Schematics illustrating the energy equipartition principle (equation 5): (a) region of interest centered along a given  $M_0$  surface, bounded left and right by two adjacent  $M$  surfaces ( $M_{-1}$  and  $M_1$ , separated by an infinitesimal  $\delta M$ ) and above and below by  $T_b$  and  $T_o$ ; (b) the corresponding region in  $(-1/2r^2, M^2)$  space; (c) the corresponding region in  $(s^*, T)$  space.

An alternative approach to calculate the  $Area_{(s^*, T)}$  is to define an area function  $A(M) = \int_{T_b}^{T_o} s^* dT$ , which is the area to the left of the  $M$  isoline between  $T_b$  and  $T_o$  (Fig. B2a,b). The area of our interest (Fig. B1c) is  $A(M_1 + \delta M) - A(M) = \delta \left( \int_{T_b}^{T_o} s^* dT \right)$ , i.e., the change in saturation entropy integral between the two  $M$  surfaces. To the first order of  $\delta M$ ,

$$\begin{aligned}
 Area_{(s^*, T)} &= \delta \left( \int_{T_b}^{T_o} s^* dT \right) = A(M_1 + \delta M) - A(M_1) \\
 &\approx \frac{d(A)}{dM} \delta M \\
 &= \frac{d}{dM} \left( \int_{T_b}^{T_o} s^* dT \right) \delta M
 \end{aligned} \tag{B4}$$

Equating  $Area_{(M^2, -1/2r^2)}$  and  $Area_{(s^*, T)}$ , we obtain

$$\frac{v_b}{r_b} = \frac{d}{dM} \left( \int_{T_b}^{T_o} s^* dT \right) \tag{B5}$$

The above two approaches are mathematically linked by the Leibniz rule of integration. We verify their equivalency by plotting  $v_b$  computed from (B.3) against (B.5) for each of the 11 members of the CTRL at  $t_{RI}$ , as shown in Fig. B2d.

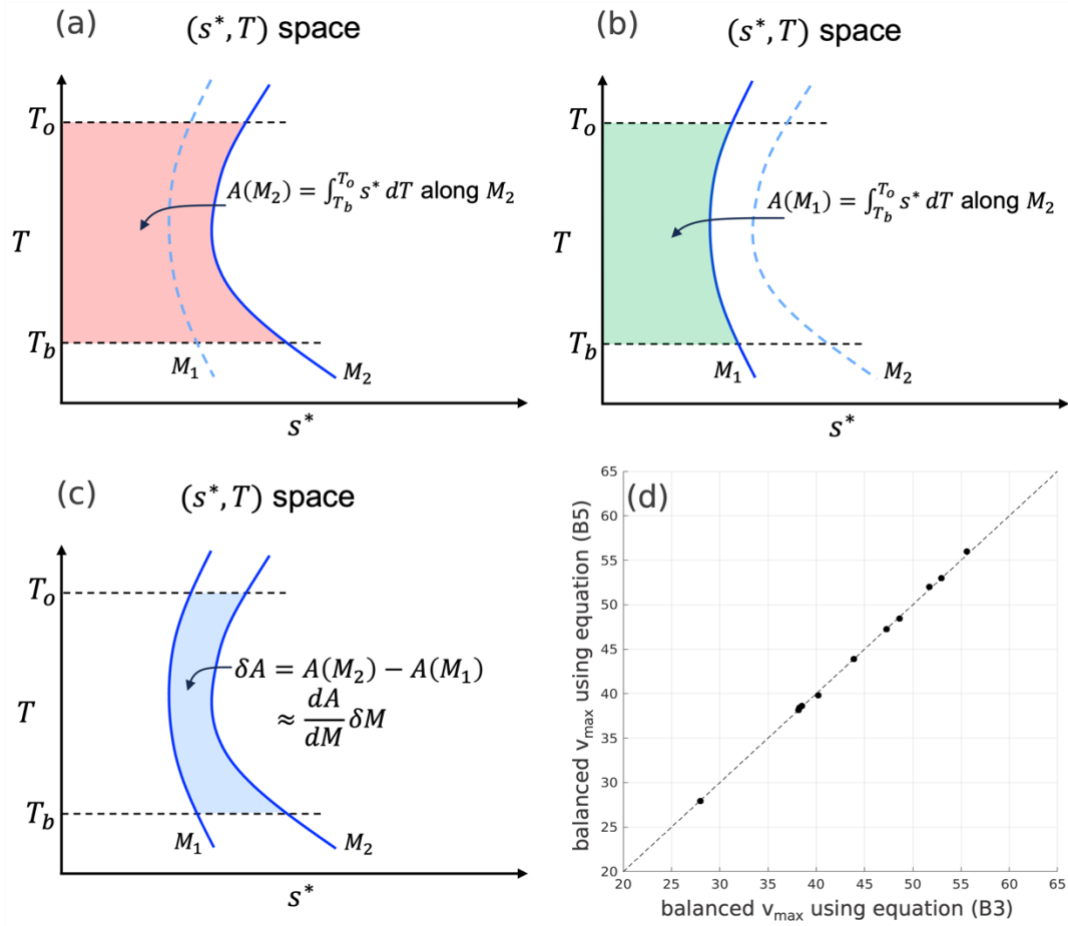


**Fig. B2:** Schematics illustrating a second method of evaluating the area of interest in  $(s^*, T)$  space: (a) the area to the left of the  $M_2$  isoline in  $(s^*, T)$  space (bounded by  $T_b$  and  $T_o$ ), which equals to  $A(M_2)$ ; (b) similar to (a), but for area represented by  $A(M_1)$ ; (c) the area of interested in  $(s^*, T)$  space, which equals to the difference between  $A(M_2)$  and  $A(M_1)$ . (d) A scattered plot showing the balanced  $v_{\max}$  evaluated from (B.5) against that from (B.3) for each CTRL member at  $t_{RI}$ .

## Appendix C: The generalized tangential wind formula in a height coordinate

In this appendix, we derive the fully generalized tangential wind formula in height coordinate, which allows us to compare with results from Lilly 1979, 1986 (unbalanced manuscripts, Tao et al. 2020) and BR09b.

The local tendency terms of the radial ( $u$ ) and vertical ( $w$ ) momentum equations are assumed to be small compared to the rest of the terms (Abarca et al. 2015) and thus are neglected. Together with the anelastic form of the continuity in  $(r, z)$  coordinate, we have

$$u \frac{\partial u}{\partial r} + w \frac{\partial u}{\partial z} = \frac{M^2}{r^3} - \frac{1}{4} f^2 r - \alpha \frac{\partial p}{\partial r} + F_r \quad (\text{C1a})$$

$$u \frac{\partial w}{\partial r} + w \frac{\partial w}{\partial z} = -g - \alpha \frac{\partial p}{\partial z} + F_z \quad (\text{C1b})$$

$$\frac{1}{r} \frac{\partial r \rho u}{\partial r} + \frac{\partial \rho w}{\partial z} = 0 \quad (\text{C1c})$$

, where  $\rho$ ,  $\alpha$  and  $p$  are the total moist air density, specific volume and pressure;  $F_r$  and  $F_z$  are the momentum forcings in the radial and vertical directions. For simplicity, we neglect the hydrometeor loading in the total density  $\rho = \rho_d + \rho_v$ , where  $\rho_v$  is vapor density. With equation (C1c),  $\mathbf{u} = (u, w)$  can be written in terms of nondivergent streamfunction  $\psi$  as  $\left( \frac{1}{r\rho} \frac{\partial \psi}{\partial z}, \frac{-1}{r\rho} \frac{\partial \psi}{\partial r} \right)$ .

Following Lilly 1979, (C1a) and (C1b) can then be rewritten as

$$\frac{\partial}{\partial r} \left( \frac{u^2 + w^2 + v^2}{2} + \frac{fM}{2} + gz \right) - \frac{\eta}{r\rho} \frac{\partial \psi}{\partial r} = \frac{1}{2r^2} \frac{\partial M^2}{\partial r} - \alpha \frac{\partial p}{\partial r} + F_r \quad (\text{C2a})$$

$$\frac{\partial}{\partial z} \left( \frac{u^2 + w^2 + v^2}{2} + \frac{fM}{2} + gz \right) - \frac{\eta}{r\rho} \frac{\partial \psi}{\partial z} = \frac{1}{2r^2} \frac{\partial M^2}{\partial z} - \alpha \frac{\partial p}{\partial z} + F_z \quad (\text{C2b})$$

, where  $\eta = \left( \frac{\partial u}{\partial z} - \frac{\partial w}{\partial r} \right)$  is the azimuthal vorticity. Defining  $\tilde{\eta} = \eta/\rho$  and cross differentiating (C2a)

and (C2b) yields

$$0 = \frac{2M}{r^3} \frac{\partial M}{\partial z} + J \left( \frac{\alpha, p}{r, z} \right) + J \left( \frac{\psi, \tilde{\eta}/r}{r, z} \right) + \frac{\partial F_r}{\partial z} - \frac{\partial F_z}{\partial r} \quad (\text{C3})$$

We note here that  $J \left( \frac{\psi, \tilde{\eta}/r}{r, z} \right) = -\frac{\partial}{\partial r} \left( \frac{\eta}{r\rho} \frac{\partial \psi}{\partial z} \right) - \frac{\partial}{\partial z} \left( -\frac{\tilde{\eta}}{r\rho} \frac{\partial \psi}{\partial r} \right) = -\nabla_{r,z} \cdot (\eta \mathbf{u})$  is the *convergence of azimuthal vorticity flux*. (C3) thus represents the balance between the centrifugal torque, the baroclinic torque, torque induced by azimuthal vorticity flux convergence and frictional torque.

Two approximations will be made to couple with saturated moist dynamics. First, we define  $s^* = c_p \ln T - R_d \ln p_d + \frac{L_v q^*}{T}$ , which satisfies  $T ds^* = c_p dT - \alpha_d dp_d + L_v dq^* - \frac{L_v q^*}{T} dT$ . A long-

standing approximation is to assume the  $-\frac{L_v q^*}{T} dT$  term being small, thus reducing it to the modified first law of thermodynamics (E86; BR09a)

$$T ds^* = c_p dT - \alpha_d dp_d + L_v dq^* \quad (\text{C4})$$

Integrating (C4) along the closed boundary  $\partial D$  of an arbitrary saturated region  $D$  within the eyewall and applying the Stoke's theorem, we have

$$(\nabla T \times \nabla s^* \cdot \hat{\lambda}) = (\nabla p_d \times \nabla \alpha_d \cdot \hat{\lambda}) \quad (\text{C5})$$

, where  $\hat{\lambda}$  is the unit vector in the azimuthal direction. Because  $\nabla T \times \nabla s^* \cdot \hat{\lambda} = J\left(\frac{s^*, T}{r, z}\right)$  and  $\nabla p_d \times \nabla \alpha_d \cdot \hat{\lambda} = J\left(\frac{\alpha_d, p_d}{r, z}\right)$ , we can rewrite (C5) as  $J\left(\frac{s^*, T}{r, z}\right) = J\left(\frac{\alpha_d, p_d}{r, z}\right)$ . The second approximation is to neglect the contributions of water vapor to the value of density and pressure, such that  $J\left(\frac{\alpha_d, p_d}{r, z}\right) = J\left(\frac{\alpha, p}{r, z}\right)$ . Therefore, (C5) becomes

$$J\left(\frac{s^*, T}{r, z}\right) = J\left(\frac{\alpha, p}{r, z}\right) \quad (\text{C6})$$

Combining (C6) with (C3), using equation (A3) to write  $J\left(\frac{\psi, \tilde{\eta}/r}{r, z}\right) = \left(\frac{\partial \psi}{\partial r}\right)_z \left(\frac{\partial \tilde{\eta}/r}{\partial z}\right)_\psi$ ,  $J\left(\frac{s^*, T}{r, z}\right) = \left(\frac{\partial T}{\partial z}\right)_{s^*} \left(\frac{\partial s^*}{\partial r}\right)_z$  and dividing both sides of (C3) with  $\left(\frac{\partial M}{\partial r}\right)_z$ , we have

$$\frac{2M}{r^3} \left(\frac{\partial r}{\partial z}\right)_M = \left(\frac{\partial T}{\partial z}\right)_{s^*} \left(\frac{\partial s^*}{\partial M}\right)_z + \left(\frac{\partial \psi}{\partial M}\right)_z \left(\frac{\partial \tilde{\eta}/r}{\partial z}\right)_\psi + \left(\frac{\partial F_r}{\partial z}\right)_r \left(\frac{\partial r}{\partial M}\right)_z - \left(\frac{\partial F_z}{\partial M}\right)_z \quad (\text{C7})$$

Using the equivalent forms of Jacobian determinant (A3), (C7) can be further rewritten as

$$\frac{2M}{r^3} \left(\frac{\partial r}{\partial z}\right)_M = \left(\frac{\partial T}{\partial z}\right)_M \left(\frac{\partial s^*}{\partial M}\right)_T + \left(\frac{\partial \psi}{\partial M}\right)_{\tilde{\eta}/r} \left(\frac{\partial \tilde{\eta}/r}{\partial z}\right)_M - \left(\frac{\partial F_r}{\partial M}\right)_r \left(\frac{\partial r}{\partial z}\right)_M - \left(\frac{\partial F_z}{\partial M}\right)_z \quad (\text{C8})$$

Integrating (C8) along an  $M$  isoline from  $z_b$  to the outflow radius at outflow level  $z_o$ , we obtain the generalized tangential wind formula in height coordinate

$$\frac{v_b}{r_b} = \int_{T_b}^{T_o} \left(\frac{\partial s^*}{\partial M}\right)_T dT + \int_{\tilde{\eta}_b/r_b}^{\tilde{\eta}_o/r_o} \left(\frac{\partial \psi}{\partial M}\right)_{\tilde{\eta}/r} d\left(\frac{\tilde{\eta}}{r}\right) - \int_{r_b}^{r_o} \left(\frac{\partial F_r}{\partial M}\right)_r dr - \int_{z_b}^{z_o} \left(\frac{\partial F_z}{\partial M}\right)_z dz \quad (\text{C9})$$

## Appendix D: Correction term to the balanced wind component

Two approximations were frequently made in the derivation of PI theory to couple the momentum equations with saturated moist thermodynamics. The first approximated is the neglect of water vapor contribution to the total density and pressure of moist air. A second (more important but often ignored) approximation is that in deriving the modified first law of thermodynamics  $Tds^* = c_p dT - \alpha_d dp_d + L_v dq^*$  from the saturation entropy  $s^* = c_p \ln T - R_d \ln p_d + \frac{L_v q^*}{T}$ , the temperature variation in the latent heat release (e.g.,  $-\frac{L_v q^*}{T} dT$ ) is assumed to be small and neglected. In this appendix, we derive correction terms to quantify the effects of the aforementioned approximations on the balanced wind component. The approach bears some similarity to Emanuel (1988), but without the complexity of deriving the Maxwell equations.

Note that  $s^*$  satisfies the following differential form

$$Tds^* = c_p dT - \alpha_d dp_d + L_v dq^* - \frac{L_v q^*}{T} dT \quad (\text{D1})$$

We integrate (D1) along the closed boundary  $\partial D$  of an arbitrary saturated region  $D$  within the saturated eyewall region. Applying the Stoke's theorem, we have

$$(\nabla T \times \nabla s^* \cdot \hat{\lambda}) = -(\nabla \alpha_d \times \nabla p_d \cdot \hat{\lambda}) - \frac{L_v}{T} (\nabla q^* \times \nabla T \cdot \hat{\lambda}) \quad (\text{D2})$$

, where  $\hat{\lambda}$  is the unit vector in the azimuthal direction. Noting that  $q^* = \frac{R_d e_s(T)}{R_v p_d}$  and using ideal gas law of water vapor, we can write the last term of (D2) as  $-\frac{L_v}{T} (\nabla q^* \times \nabla T \cdot \hat{\lambda}) = -\frac{L_v q^*}{R_d T} (\nabla \alpha_d \times \nabla p_d \cdot \hat{\lambda})$ . Thus, (D2) can be rewritten as

$$(\nabla T \times \nabla s^* \cdot \hat{\lambda}) = \left(1 + \frac{L_v q^*}{R_d T}\right) (\nabla p_d \times \nabla \alpha_d \cdot \hat{\lambda}) \quad (\text{D3})$$

Furthermore, negelecting the effect of hydrometeor loading, we write  $p = p_d + e_s(T)$ ,  $\rho = \rho_d + \rho_v^*(T)$ , so that  $\alpha = (\rho_d + \rho_v^*)^{-1} \approx \alpha_d + \alpha'$  with  $\alpha' := -\frac{\rho_v^*}{\rho_d} \alpha_d$ . Together with the Clausius–Clapeyron equation  $\frac{de_s}{dT} = \frac{L_v e_s}{R_v T^2}$ , we can show that to the zeroth order of  $q^*$  ( $= \frac{\rho_v^*}{\rho_d}$ )

$$\begin{aligned} (\nabla p \times \nabla \alpha \cdot \hat{\lambda}) &\approx (\nabla p_d \times \nabla \alpha_d \cdot \hat{\lambda}) \left(1 - q^* + \frac{L_v q^*}{R_d T} \left(1 - \frac{R_d}{R_v} - 2q^*\right)\right) \\ &\approx (\nabla p_d \times \nabla \alpha_d \cdot \hat{\lambda}) \left(1 + \frac{L_v q^*}{R_d T} \left(1 - \frac{R_d}{R_v}\right)\right) \end{aligned} \quad (\text{D4})$$

Because  $\nabla T \times \nabla s^* \cdot \hat{\lambda} = J\left(\frac{s^*, T}{r, z}\right)$  and  $\nabla p \times \nabla \alpha \cdot \hat{\lambda} = J\left(\frac{\alpha, p}{r, z}\right)$ , we use (D4) to rewrite (D3) as

$$J\left(\frac{\alpha, p}{r, z}\right) = J\left(\frac{s^*, T}{r, z}\right)(1 - \gamma) \quad (\text{D5})$$

, where  $\gamma = \frac{R_r \beta}{1 + \beta}$  with  $\beta = \frac{L_v q^*}{R_d T}$  and  $R_r = \frac{R_d}{R_v} \approx 0.622$ . This relation is the corrected version of (C5) in appendix C. Using (D5) and continuing the derivation in appendix C, we can obtain the following version of generalized tangential wind formula

$$\frac{v_b}{r_b} = \int_{\tilde{T}_b}^{T_o} \left(\frac{\partial s^*}{\partial M}\right)_T dT + \int_{\tilde{\eta}_b/r_b}^{\tilde{\eta}_o/r_o} \left(\frac{\partial \psi}{\partial M}\right)_{\tilde{\eta}/r} d\left(\frac{\tilde{\eta}}{r}\right) - \int_{r_b}^{r_o} \left(\frac{\partial F_r}{\partial M}\right)_r dr - \int_{z_b}^{z_o} \left(\frac{\partial F_z}{\partial M}\right)_z dz - \int_{\tilde{T}_b}^{T_o} \gamma \left(\frac{\partial s^*}{\partial M}\right)_T dT \quad (\text{D6})$$

The last term  $-\int_{\tilde{T}_b}^{T_o} \gamma \left(\frac{\partial s^*}{\partial M}\right)_T dT$  is the correction term for the balanced component to account for the impacts of (1) the temperature variation on the latent heat release, and (2) the inclusion of water vapor in the total density and pressure. This correction term is true only under saturation condition.

## Appendix E: Regularization of singularity in $\left(\frac{\partial s^*}{\partial M}\right)_T$ and $\left(\frac{\partial \psi}{\partial M}\right)_{\bar{\eta}}$

In this appendix, we document the treatment to singularities of  $\left(\frac{\partial s^*}{\partial M}\right)_T$  and  $\left(\frac{\partial \psi}{\partial M}\right)_{\bar{\eta}}$  along the integration path when they occur. The following discussion will only focus on  $\left(\frac{\partial s^*}{\partial M}\right)_T$  for simplicity, since the same reasoning can also be applied to analyze the  $\left(\frac{\partial \psi}{\partial M}\right)_{\bar{\eta}}$  term.

From the definition  $\left(\frac{\partial s^*}{\partial M}\right)_T := \lim_{\substack{\delta M \rightarrow 0 \\ T = \text{const}}} \frac{\delta s^*}{\delta M}$ , we can see that the necessary and sufficient condition for the occurrence of singularity is when  $\delta M$  becomes *identically zero* when holding  $T$  constant, which happens if and only if the isolines of  $M$  and  $T$  are parallel at a grid point. However, since our interest is the integral  $\int \left(\frac{\partial s^*}{\partial M}\right)_T dT$ , I will show that  $\int \left(\frac{\partial s^*}{\partial M}\right)_T dT$  remains integrable even if  $\left(\frac{\partial s^*}{\partial M}\right)_T$  may have (a finite number of) singularities along the integration path. First, we note that at the singularity where  $M$  and  $T$  isolines are parallel,  $dT$  must also be 0. As such, the integrand  $\left(\frac{\partial s^*}{\partial M}\right)_T dT$  must be in an indeterminate form of  $\infty \times 0$  at the point of singularity. This means we can regularize the singularity if this indeterminate form has a finite limit.

To show this, we will first change the variable of integration to something that always has non-zero finite differential along the integration path. The natural choice of such a variable is the path length, denoted as  $l$ . First, we construct the natural coordinate along the integration path (an  $M$  isoline), denoted by the unit vectors  $(\hat{n}, \hat{l})$ . Specifically, we define  $\hat{n} = \frac{\nabla M}{|\nabla M|}$  to be the unit vector perpendicular to the  $M$  isoline, while  $\hat{l} := \hat{n} \times \hat{\lambda}$  is the direction along the  $M$  isoline ( $\hat{\lambda}$  is the tangential direction). Note that the two unit vectors  $(\hat{n}, \hat{l})$  form a local cartesian coordinate  $(n, l)$  of unit grid size in  $(r, z)$  space. We now consider the integral of  $\left(\frac{\partial s}{\partial M}\right)_T$  across the interval  $\left(T_i - \frac{\delta T}{2}, T_i + \frac{\delta T}{2}\right)$  where the singularity lies. We can write this integral using the natural coordinate as

$$\begin{aligned} \int_{T_i - \frac{\delta T}{2}}^{T_i + \frac{\delta T}{2}} \left(\frac{\partial s}{\partial M}\right)_T dT &= \int_{l_i - \frac{\delta l}{2}}^{l_i + \frac{\delta l}{2}} \left(\frac{\partial s}{\partial M}\right)_T \left(\frac{\partial T}{\partial l}\right)_M dl \\ &= \int_{l_i - \frac{\delta l}{2}}^{l_i + \frac{\delta l}{2}} \left(\frac{\partial s}{\partial M}\right)_l \left(\frac{\partial T}{\partial l}\right)_s dl \end{aligned}$$

$$= \int_{l_i - \frac{\delta l}{2}}^{l_i + \frac{\delta l}{2}} \left( \frac{\partial n}{\partial M} \right)_l \left( \frac{\partial s}{\partial n} \right)_l \left( \frac{\partial T}{\partial l} \right)_s dl \quad (\text{E1})$$

where  $(l_i - \frac{\delta l}{2}, l_i + \frac{\delta l}{2})$  is the incremental line segment of the integration path. The second equality uses the Jacobian identity (A.3) that  $(\frac{\partial s}{\partial M})_T (\frac{\partial T}{\partial l})_M = (\frac{\partial s}{\partial M})_l (\frac{\partial T}{\partial l})_s$ . Note that by definition  $(\frac{\partial M}{\partial n})_l \equiv |\nabla M|$  and that  $(\frac{\partial s}{\partial n})_l (\frac{\partial T}{\partial l})_s$  is the Jacobian  $J(\frac{s^*, T}{n, l})$ , which also equals to  $J(\frac{s^*, T}{r, z})$  because  $J(\frac{n, l}{r, z}) =$

1. Therefore, we can rewrite (E.1) as

$$\int_{T_i - \frac{\delta T}{2}}^{T_i + \frac{\delta T}{2}} \left( \frac{\partial s}{\partial M} \right)_T dT = \int_{l_i - \frac{\delta l}{2}}^{l_i + \frac{\delta l}{2}} \frac{1}{|\nabla M|} J(\frac{s^*, T}{r, z}) dl \quad (\text{E2})$$

Within the vortex region,  $dl$  and  $J(\frac{s^*, T}{r, z})$  are both finite and  $|\nabla M|$  is always non-zero. This thus shows that  $(\frac{\partial s}{\partial M})_T dT$  indeed has a finite limit, which equals to  $\frac{1}{|\nabla M|} J(\frac{s^*, T}{r, z}) dl$ . We now define the

regularization of  $(\frac{\partial s}{\partial M})_T$  (denoted as  $(\overline{\frac{\partial s}{\partial M}})_T$ ) as  $(\overline{\frac{\partial s}{\partial M}})_T := \frac{1}{\delta T} \int_{T_i - \frac{\delta T}{2}}^{T_i + \frac{\delta T}{2}} (\frac{\partial s}{\partial M})_T dT$ . Given (E.2), we

have

$$(\overline{\frac{\partial s}{\partial M}})_T = \frac{1}{\delta T} \int_{l_i - \frac{\delta l}{2}}^{l_i + \frac{\delta l}{2}} J(\frac{s^*, T}{r, z}) \frac{dl}{|\nabla M|} \quad (\text{E3})$$

Close examination of (E.3) found (not shown) that when singularity does not occur,  $(\overline{\frac{\partial s}{\partial M}})_T$  equals to the mean value of  $(\frac{\partial s}{\partial M})_T$  over the interval  $(T_i - \frac{\delta T}{2}, T_i + \frac{\delta T}{2})$ ; while at intervals where singularity lies, it allows accurate integration across the singularity. Similarly,  $(\frac{\partial \psi}{\partial M})_{\tilde{\eta}}$  can be regularized as

$$(\overline{\frac{\partial \psi}{\partial M}})_{\tilde{\eta}/r} := \frac{1}{\delta(\tilde{\eta}/r)} \int_{l_i - \frac{\delta l}{2}}^{l_i + \frac{\delta l}{2}} J(\frac{\psi, \tilde{\eta}/r}{r, z}) \frac{dl}{|\nabla M|} \quad (\text{E4})$$

Supplementary material S1: Derivation using the approach of Lilly 1979, 1986

The derivation of equation (11) in the main manuscript follows the approach of Emanuel (1986) (as in Appendix C). It is possible to derive the main findings using an alternative approach from Lilly 1979, 1986 (unpublished manuscript; Tao et al. 2020).

Neglecting local time tendency of radial and vertical velocities, the radial and vertical momentum equations and the anelastic form of the continuity in  $(r, z)$  coordinate are

$$u \frac{\partial u}{\partial r} + w \frac{\partial u}{\partial z} = \frac{v^2}{r} + fv - \alpha \frac{\partial p}{\partial r} + F_r \quad (\text{S1.1a})$$

$$u \frac{\partial w}{\partial r} + w \frac{\partial w}{\partial z} = -g - \alpha \frac{\partial p}{\partial z} + F_z \quad (\text{S1.1b})$$

$$\frac{1}{r} \frac{\partial r \rho u}{\partial r} + \frac{\partial \rho w}{\partial z} = 0 \quad (\text{S1.1c})$$

Writing  $\mathbf{u} = (u, w)$  as  $\left(\frac{1}{r\rho_d} \frac{\partial \psi}{\partial z}, \frac{-1}{r\rho_d} \frac{\partial \psi}{\partial r}\right)$ , (S1.1a) and (S1.1b) can be rewritten into the following forms (as in Lilly 1979):

$$\frac{\partial}{\partial r} \left( \frac{u^2 + w^2 + v^2}{2} + \frac{fM}{2} + gz \right) = \frac{\eta}{r\rho} \frac{\partial \psi}{\partial r} + \frac{1}{2r^2} \frac{\partial M^2}{\partial r} - \alpha \frac{\partial p}{\partial r} + F_r \quad (\text{S1.2a})$$

$$\frac{\partial}{\partial z} \left( \frac{u^2 + w^2 + v^2}{2} + \frac{fM}{2} + gz \right) = \frac{\eta}{r\rho} \frac{\partial \psi}{\partial z} + \frac{1}{2r^2} \frac{\partial M^2}{\partial z} - \alpha \frac{\partial p}{\partial z} + F_z \quad (\text{S1.2b})$$

, where  $\eta = \frac{\partial u}{\partial z} - \frac{\partial w}{\partial r}$  is the azimuthal vorticity. The L.H.S of (S1.2a) and (S1.2b) are the

*conservative components* of the advection term and effective gravity  $\left(\frac{v^2}{r} + fv, -g\right)$ ; Smiths et al. 2005), whereas the R.H.S terms are the *nonconservative components* of advection (1<sup>st</sup> term), centrifugal force (2<sup>nd</sup> term) and pressure gradient force (3<sup>rd</sup> term), as well as radial and vertical momentum forcings (4<sup>th</sup> term). (S1.2a) and (S1.2b) can be combined into one vector equation in the  $(r, z)$  plane

$$\nabla \left( \frac{u^2 + w^2 + v^2}{2} + \frac{fM}{2} + gz \right) = \frac{\eta}{r\rho} \nabla \psi + \frac{1}{2r^2} \nabla M^2 - \alpha \nabla p + \mathbf{F} \quad (\text{S1.3})$$

, where  $\nabla = \frac{\partial}{\partial r} \hat{r} + \frac{\partial}{\partial z} \hat{z}$  and  $\mathbf{F} = F_r \hat{r} + F_z \hat{z}$ . To couple with moist thermodynamics, we define  $s^* = c_p \ln T - R_d \ln p + \frac{L_v q^*}{T}$  and take the gradient operator on both sides. Neglecting  $T$  variation in the last term and assuming  $\alpha \approx R_d T / p$ , we have

$$T \nabla s^* \approx c_p \nabla T - \alpha \nabla p + L_v \nabla q^* \quad (\text{S1.4})$$

Cancelling  $\alpha \nabla p$  in (S1.3) and (S1.4), we have

$$\nabla \left( \frac{u^2 + w^2 + v^2}{2} + \frac{fM}{2} + gz + c_p T + L_v q^* + Ts^* \right) = \frac{\eta}{r\rho} \nabla \psi + \frac{1}{2r^2} \nabla M^2 - s^* \nabla T + \mathbf{F} \quad (\text{S1.5})$$

Consider an arbitrary connected region  $D$  within the saturated eyewall updraft, if we take the dot-product of each term in (S1.5) with  $d\mathbf{l}$  and integrate along the closed loop  $\partial D$ , the conservative force component on the L.H.S vanishes, resulting in a balance between the loop integral of the non-conservative force components

$$\oint \frac{1}{2r^2} \nabla M^2 \cdot d\mathbf{l} = \oint s^* \nabla T \cdot d\mathbf{l} + \oint -\frac{\eta}{r\rho} \nabla \psi \cdot d\mathbf{l} - \oint \mathbf{F} \cdot d\mathbf{l} \quad (\text{S1.6a})$$

$$= \oint s^* \nabla T \cdot d\mathbf{l} + \oint \eta \mathbf{u} \cdot (-\hat{\mathbf{n}}) dl - \oint \mathbf{F} \cdot d\mathbf{l} \quad (\text{S1.6b})$$

It is shown in (S.16b) that the nonlinear advection term (2<sup>nd</sup> term on the R.H.S) can also be written in the form of inward flux of azimuthal vorticity  $\eta$  through the close loop  $\partial D$ . Using Stoke's theorem on (S1.6) and dropping the double integral (due to the arbitrary nature of  $D$ ) yields

$$\nabla \left( \frac{1}{2r^2} \right) \times \nabla M^2 \cdot \hat{\lambda} = \nabla s^* \times \nabla T \cdot \hat{\lambda} - \nabla \left( \frac{\eta}{r\rho} \right) \times \nabla \psi \cdot \hat{\lambda} - \nabla \times \mathbf{F} \cdot \hat{\lambda} \quad (\text{S1.7a})$$

$$= \nabla s^* \times \nabla T \cdot \hat{\lambda} - \nabla \cdot (\eta \mathbf{u}) - \nabla \times \mathbf{F} \cdot \hat{\lambda} \quad (\text{S1.7b})$$

Because  $\nabla \alpha \times \nabla \beta \cdot \hat{\lambda} = J \left( \frac{\beta, \alpha}{r, z} \right)$ , we can obtain equation (C3) in appendix C using the fact that  $J \left( \frac{s^*, T}{r, z} \right) = J \left( \frac{\alpha, p}{r, z} \right)$ . This shows that the approach of Lilly (1979), (1986) is equivalent to that of Emanuel (1986).

In addition to using Jacobian properties in the manuscript, one of the reviewers also noticed that equation (9) can be derived by directly expanding the loop integration in (S1.6). To do this, we consider a narrow region  $D$ , bounded between the  $M_0$ ,  $M_0 + \delta M$  surfaces,  $T_b$  and  $T_o$ , as shown in Fig. S1. Without loss of generality,  $T_b(M)$  and  $T_o(M)$  are both functions of  $M$ . In addition, we require that  $r_o$  and  $T_o$  at the  $M_0$  surface to be the radius and temperature where the tangential wind  $v$  of the  $M_0$  surface equals to 0. However, we *do not require*  $r_o$  and  $T_o$  at the  $M_0 + \delta M$  to satisfy  $v = 0$ . If we perform a loop integral for the L.H.S of (S1.6), we see that path (1) and (3) are identically zero due to  $dM^2 = 0$  on these path. To the first order of  $\delta M$ , we have

$$\begin{aligned} \oint \frac{1}{2r^2} \nabla M^2 \cdot d\mathbf{l} &= \int_{M_0^2}^{(M_0 + \delta M)^2} \frac{1}{2r_b^2(M)} dM^2 - \int_{M_0^2}^{(M_0 + \delta M)^2} \frac{1}{2r_o^2(M)} dM^2 \\ &\approx \frac{2M_0 \delta M}{2r_b^2(M_0)} - \frac{2M_0 \delta M}{2r_o^2(M_0)} = \frac{v_b(M_0)}{r_b(M_0)} \delta M \end{aligned} \quad (\text{S1.8})$$

For the first term on the R.H.S of (S1.6), to the first order of  $\delta M$ , it may be expanded as

$$\oint s^* \nabla T \cdot d\mathbf{l} = \int_{T_b(M_0)}^{T_b(M_0+\delta M)} s_b^*(M, T_b) dT + \int_{T_b(M_0+\delta M)}^{T_o(M_0+\delta M)} s^*(M_0 + \delta M, T) dT - \int_{T_o(M_0)}^{T_o(M_0+\delta M)} s_o^*(M, T_o) dT - \int_{T_b(M_0)}^{T_o(M_0)} s_o^*(M_0, T) dT \quad (\text{S1.9a})$$

$$\approx s_b^*(M_0, T_b) \delta T_b + \int_{T_b(M_0+\delta M)}^{T_o(M_0+\delta M)} s^*(M_0, T) dT + \int_{T_b(M_0+\delta M)}^{T_o(M_0+\delta M)} \left( \frac{\partial s^*}{\partial M} \right)_T \delta M dT - s_o^*(M_0, T_o) \delta T_o \quad (\text{S1.9b})$$

$$- \int_{T_b(M_0)}^{T_o(M_0)} s_o^*(M_0, T) dT$$

, where  $\delta T_b$  and  $\delta T_o$  are changes in  $T_b$  and  $T_o$  between  $M$  and  $M + \delta M$ , which can be expressed as  $\delta T_b \approx \frac{dT_b}{dM} \delta M$  and  $\delta T_o \approx \frac{dT_o}{dM} \delta M$  and are of order  $\mathcal{O}(\delta M)$ . The second term of (S1.9b) can be

further expanded into three segments

$$\int_{T_b(M_0+\delta M)}^{T_o(M_0+\delta M)} s^*(M_0, T) dT = \int_{T_b(M_0+\delta M)}^{T_b(M_0)} s^*(M_0, T) dT + \int_{T_b(M_0)}^{T_o(M_0)} s^*(M_0, T) dT + \int_{T_o(M_0)}^{T_o(M_0+\delta M)} s^*(M_0, T) dT \approx -s^*(M_0, T_b) \delta T_b + \int_{T_b(M_0)}^{T_o(M_0)} s^*(M_0, T) dT + s^*(M_0, T_o) \delta T_o \quad (\text{S1.10})$$

Note that these three terms of (S1.10) cancels out with the first, forth and third terms in (S1.9b), respectively. Therefore, (S1.9b) can be simplified as

$$\oint s^* \nabla T \cdot d\mathbf{l} = \delta M \int_{T_b(M_0)}^{T_o(M_0)} \left( \frac{\partial s^*}{\partial M} \right)_T dT \quad (\text{S1.11})$$

, which is the same as equation (9) in the manuscript. The same procedure can be performed for the second and third terms of (S1.6). Then, dividing both sides with  $\delta M$  and obtain the same form of (11a).

In addition, if we further assume  $T_o$  and  $T_b$  to be *constant* (determined based on the upper and lower bounds of  $M_0$  surface), then the first and third integral of (S1.9a) becomes zero

$$\oint s^* \nabla T \cdot d\mathbf{l} = \int_{T_b}^{T_o} s^*(M_0 + \delta M, T) dT - \int_{T_b}^{T_o} s_o^*(M_0, T) dT = \delta \left( \int_{T_b}^{T_o} s_o^*(M, T) dT \right) \Bigg|_{M_0} \quad (\text{S1.12})$$

where  $\cdot|_{M_0}$  denotes evaluation at  $M_0$ . Note that even if we choose  $T_o$  and  $T_b$  to be constant, the result of (S1.8) is not affected. Therefore, combining (S1.12) and (S1.8), dividing both sides with  $\delta M$  and taking the limit of  $\delta M \rightarrow 0$ , then for the balanced case, we have

$$\frac{v_b(M_0)}{r_b(M_0)} = \lim_{\delta M \rightarrow 0} \frac{\delta \left( \int_{T_b}^{T_o} s_o^*(M, T) dT \right) \Big|_{M_0}}{\delta M} = \frac{d}{dM} \left( \int_{T_b}^{T_o} s_o^*(M, T) dT \right) \Big|_{M_0} \quad (\text{S1.13})$$

Since  $M_0$  is arbitrary, we have  $\frac{v_b(M)}{r_b(M)} = \frac{d}{dM} \left( \int_{T_b}^{T_o} s_o^*(M, T) dT \right)$ .

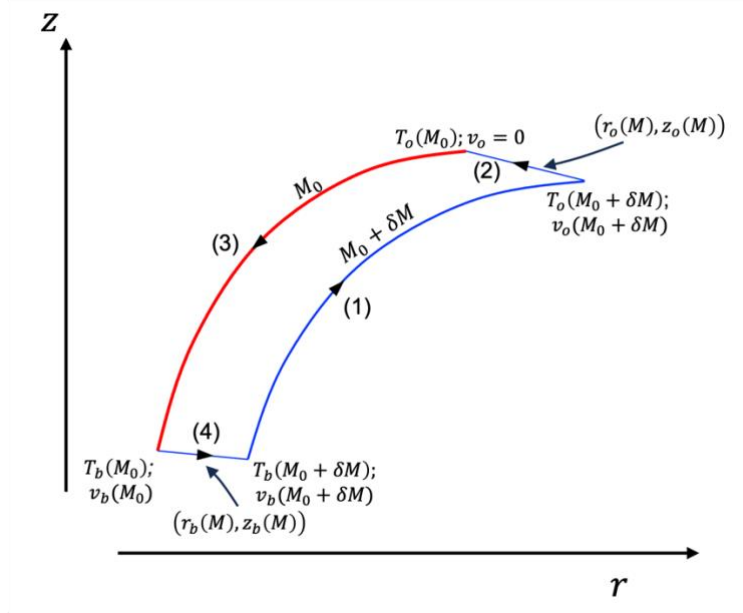


Fig. S1: Schematic of the loop integral, defined based on the  $M_0$  surface (red). The  $M_0 + \delta M$  is a neighboring  $M$  surface near the  $M_0$ , with infinitesimal  $\delta M$ . Note that we define  $r_o(M_0)$  and  $T_o(M_0)$  to satisfy  $v_o(M_0) = 0$ , while placing no constraint on  $v_o$  on any other  $M$  values. In addition, we also place no constraint on the choice of paths (2) and (4), i.e.,  $(r_o(M), z_o(M))$  and  $(r_b(M), z_b(M))$  can be any paths that passes through  $(r_o(M_0), z_o(M_0))$  and  $(r_b(M_0), z_b(M_0))$ .

## References:

- Abarca, S. F., M. T. Montgomery, and J. C. McWilliams (2015), The azimuthally averaged boundary layer structure of a numerically simulated major hurricane, *J. Adv. Model. Earth Syst.*.
- Bister, M., and K. A. Emanuel, 1998: Dissipative heating and hurricane intensity. *Meteor. Atmos. Phys.*, 65, 233–240.
- Bryan, G. H., and J. M. Fritsch, 2002: A Benchmark Simulation for Moist Nonhydrostatic Numerical Models. *Mon. Wea. Rev.*, 130, 2917–2928.
- Bryan, G. H., 2008: On the computation of pseudoadiabatic entropy and equivalent potential temperature. *Mon. Wea. Rev.*, 136, 5239–5245.
- Bryan, G. H., and R. Rotunno, 2009a: The maximum intensity of tropical cyclones in axisymmetric numerical model simulations. *Mon. Wea. Rev.*, 137, 1770–1789.
- Bryan, G. H., and R. Rotunno, 2009b: Evaluation of an Analytical Model for the Maximum Intensity of Tropical Cyclones. *J. Atmos. Sci.*, 66, 3042–3060.
- Bryan, G. H., 2012: Effects of Surface Exchange Coefficients and Turbulence Length Scales on the Intensity and Structure of Numerically Simulated Hurricanes. *Mon. Wea. Rev.*, 140, 1125–1143.
- Carter, Ashley H. (2001). *Classical and Statistical Thermodynamics*. Prentice Hall. p. 392. ISBN 0-13-779208-5.
- DesRosiers, A. J., Bell, M. M., Klotzbach, P. J., Fischer, M. S., & Reasor, P. D. (2023). Observed relationships between tropical cyclone vortex height, intensity, and intensification rate. *Geophysical Research Letters*, 50, e2022GL101877.
- Dunion, J. P., 2011: Rewriting the climatology of the tropical North Atlantic and Caribbean Sea atmosphere. *J. Climate*, 24, 893–908.
- Drennan, W. M., J. A. Zhang, J. R. French, C. McCormick, and P. G. Black, 2007: Turbulent fluxes in the hurricane boundary layer. Part II: Latent heat flux. *J. Atmos. Sci.*, 64, 1103–1115.
- Emanuel, K. A., 1986: An air–sea interaction theory for tropical cyclones. Part I: Steady-state maintenance. *J. Atmos. Sci.*, 43, 585–605.
- Emanuel, K. A., 1988: The maximum intensity of hurricanes. *J. Atmos. Sci.*, 43, 1143–1155.
- Emanuel, K. A., 1994: *Atmospheric Convection*. Oxford, 580 pp.

- Emanuel, K. A., and R. Rotunno, 2011: Self-stratification of tropical cyclone outflow. Part I: Implications for storm structure. *J. Atmos. Sci.*, 68, 2236–2249.
- Emanuel, K., 2012: Self-Stratification of Tropical Cyclone Outflow. Part II: Implications for Storm Intensification. *J. Atmos. Sci.*, 69, 988–996.
- Eliassen, A., 1952: Slow Thermally or Frictionally Controlled Meridional Circulation in a Circular Vortex. *Astrophys. Norv.*, 5, 60 pp.
- Fairall, C. W., E. F. Bradley, J. E. Hare, A. A. Grachev, and J. B. Edson, 2003: Bulk Parameterization of Air–Sea Fluxes: Updates and Verification for the COARE Algorithm. *J. Climate*, 16, 571–591.
- Fischer, M. S., P. D. Reasor, R. F. Rogers, and J. F. Gamache, 2022: An Analysis of Tropical Cyclone Vortex and Convective Characteristics in Relation to Storm Intensity Using a Novel Airborne Doppler Radar Database. *Mon. Wea. Rev.*, 150, 2255–2278, <https://doi.org/10.1175/MWR-D-21-0223.1>.
- Fischer, M. S., P. D. Reasor, J. P. Dunion, and R. F. Rogers, 2025: Are Rapidly Intensifying Tropical Cyclones Associated with Unique Vortex and Convective Characteristics?. *Mon. Wea. Rev.*, 153, 183–203, <https://doi.org/10.1175/MWR-D-24-0118.1>.
- Hisashi Ozawa & Shinya Shimokawa (2015) Thermodynamics of a tropical cyclone: generation and dissipation of mechanical energy in a self-driven convection system, *Tellus A: Dynamic Meteorology and Oceanography*, 67:1, 24216, DOI: 10.3402/tellusa.v67.24216
- Montgomery, M. T., and R. K. Smith, 2017: Recent development in the fluid dynamics of the tropical cyclones. *Annu. Rev. Fluid Mech.*, 49, 541–574, <https://doi.org/10.1146/annurev-fluid-010816-060022>.
- Peng, K., R. Rotunno, and G. H. Bryan, 2018: Evaluation of a timedependent model for the intensification of tropical cyclones. *J. Atmos. Sci.*, 75, 2125–2138.
- Peng, K., R. Rotunno, G. H. Bryan, and J. Fang, 2019: Evolution of an Axisymmetric Tropical Cyclone before Reaching Slantwise Moist Neutrality. *J. Atmos. Sci.*, 76, 1865–1884.
- Persing, J., Montgomery, M. T., McWilliams, J. C., and Smith, R. K., 2013: Asymmetric and axisymmetric dynamics of tropical cyclones, *Atmos. Chem. Phys.*, 13, 12299–12341, <https://doi.org/10.5194/acp-13-12299-2013>.

- Rotunno, R., and K. A. Emanuel, 1987: An air–sea interaction theory for tropical cyclones. Part II: Evolutionary study using a nonhydrostatic axisymmetric numerical model. *J. Atmos. Sci.*, 44, 542–561.
- Rotunno, R., 2022: Supergradient Winds in Simulated Tropical Cyclones. *J. Atmos. Sci.*, 79, 2075–2086, <https://doi.org/10.1175/JAS-D-21-0306.1>.
- Schubert, W. H., and J. J. Hack, 1983: Transformed Eliassen Balanced Vortex Model. *J. Atmos. Sci.*, 40, 1571–1583.
- Schubert, W. H., S. A. Hausman, M. Garcia, K. V. Ooyama, and H. Kuo, 2001: Potential Vorticity in a Moist Atmosphere. *J. Atmos. Sci.*, 58, 3148–3157, [https://doi.org/10.1175/1520-0469\(2001\)058<3148:PVIAMA>2.0.CO;2](https://doi.org/10.1175/1520-0469(2001)058<3148:PVIAMA>2.0.CO;2).
- Smith, R. K., M. T. Montgomery, and S. Vogl, 2008: A critique of Emanuel's hurricane model and potential intensity theory. *Quart. J. Roy. Meteor. Soc.*, 134, 551–561.
- Smith, R. K., M. T. Montgomery, H. Zhu, 2005: Buoyancy in tropical cyclones and other rapidly rotating atmospheric vortices, *Dynamics of Atmospheres and Oceans*, 40, 189-208, <https://doi.org/10.1016/j.dynatmoce.2005.03.003>.
- Tao, D., R. Rotunno, and M. Bell, 2020: Lilly’s Model for Steady-State Tropical Cyclone Intensity and Structure. *J. Atmos. Sci.*, 77, 3701–3720.
- Tang, B., and K. Emanuel, 2010: Midlevel ventilation’s constraint on tropical cyclone intensity. *J. Atmos. Sci.*, 67, 1817–1830, doi:10.1175/2010jas3318.1.
- Tang, B., and K. Emanuel, 2012a: Sensitivity of tropical cyclone intensity to ventilation in an axisymmetric model. *J. Atmos. Sci.*, 69, 2394–2413, doi:10.1175/jas-d-11-0232.1.
- Tang, B., and K. Emanuel, 2012b: A ventilation index for tropical cyclones. *Bull. Amer. Meteor. Soc.*, 93, 1901–1912, doi:10.1175/bams-d-11-00165.1.
- Wang, D., Y. Lin, and D. R. Chavas, 2022: Tropical Cyclone Potential Size. *J. Atmos. Sci.*, 79, 3001–3025.
- Wang, Y., Y. Li, J. Xu, Z. Tan, and Y. Lin, 2021a: The Intensity Dependence of Tropical Cyclone Intensification Rate in a Simplified Energetically Based Dynamical System Model. *J. Atmos. Sci.*, 78, 2033–2045.
- Wang, Y., Y. Li, and J. Xu, 2021b: A New Time-Dependent Theory of Tropical Cyclone Intensification. *J. Atmos. Sci.*, 78, 3855–3865.